Highly scaled measurements of *C. elegans* development suggest that physical constraints guide growth trajectories and animal shape

Joy Nyaanga[1,2], Christina Goss[3], Gaotian Zhang[1], Hannah N. Ahmed[1], Elliot J. Andersen[1], Isabella R. Miller[1], Justine K. Rozenich[1], Iris L. Swarthout[1], Jordan A. Vaughn[1], Erik C. Andersen[1], Niall M. Mangan[3], and Sasha Shirman[3]

1. Department of Molecular Biosciences, Northwestern University, Evanston, IL 60208, USA

2. Interdisciplinary Biological Sciences Program, Northwestern University, Evanston, IL 60208, USA

3. Department of Engineering Sciences and Applied Mathematics, Northwestern University, Evanston, IL 60208, USA

Keywords: Developmental growth; growth control; *C. elegans*; feeding dynamics; growth dynamics; stretcher model

Emails and ORCIDs:
JN: JoyNyaanga2024@u.northwestern.edu, 0000-0002-1402-9213
CG: christinagoss2021@u.northwestern.edu, 0000-0002-5715-3337
GZ: gaotian.zhang@northwestern.edu, 0000-0001-6468-1341
HNA: hannahahmed02@gmail.com
EJA: elliotjandersen@gmail.com
IRM: miller.ir18@gmail.com
JKR: justine.rozenich@icloud.com
ILS: IrisSwarthout2023@u.northwestern.edu
JAV: JordanVaughn2023@u.northwestern.edu
ECA: erik.andersen@gmail.com, 0000-0003-0229-9651
NMM: niallmm@gmail.com, 0000-0002-3491-8341
SS: shirman.sasha@gmail.com, 0000-0001-5855-9470

Abstract

Growth control establishes organism size, requiring mechanisms to sense and adjust growth. Studies of single cells revealed that size homeostasis uses distinct control methods: Size, Timer, and Adder. In multicellular organisms, mechanisms that regulate single cell growth must integrate control across organs and tissues during development to generate adult size and shape. We leveraged the roundworm *Caenorhabditis elegans* as a scalable and tractable model to collect precise growth measurements of thousands of individuals, measure feeding behavior, and quantify changes in animal size and shape. Using quantitative measurements and mathematical modeling, we propose two models of physical mechanisms by which *C. elegans* can control growth. First, constraints on cuticle stretch generate mechanical signals through which animals sense body size and initiate larval-stage transitions. Second, mechanical control of food intake drives growth rate within larval stages. These results suggest how physical constraints control developmental timing and growth rate in *C. elegans*.

Introduction

Growth is a complex process fundamental to development. Individual cells and whole animals must reach an appropriate size to remain competitive in their environment. A larger body size conveys many selective advantages to an organism, including increased predation success or defense against predation, increased success in mating, and increased success in intraspecific as well as interspecific competition. Offsetting these advantages, larger organisms require more food resources to grow, take longer to develop, and produce fewer offspring (Hone and Benton, 2005). Therefore, it is critical for multicellular organisms to effectively coordinate the growth of both individual cells and the whole body. Additionally, growth at both of these scales must be coupled with developmental progression to ensure the proper timing of irreversible developmental events.

In recent years, efforts have focused on understanding how organisms control growth to achieve size homeostasis (Björklund, 2019; Turner et al., 2012; Willis and Huang, 2017). Many of these studies are motivated by the decades-long debate about whether growth is linear or exponential; two separate models each having unique implications for size regulation. In a linear model with constant growth rate, smaller organisms must grow proportionally more than larger organisms to maintain size homeostasis. In this paradigm, organism size can be controlled simply by specifying growth duration. Subsequently, this method of growth control was named the 'Timer' model (Donnan and John, 1983; Wang et al., 2000). Instead of regulating growth duration, organisms can monitor size and adjust duration of growth to reach an optimal size, often named the 'Sizer' model (Pavelescu et al., 2018; Sveiczer et al., 1996; Tzur et al., 2009). In an exponential model, growth rate is proportional to size. Here, a time-based control mechanism alone would fail to maintain size homeostasis because larger organisms would grow proportionally more during a specified period of time. This difference in growth requires a size-based control mechanism to ensure that growth is halted once a maximum size is reached. Although 'Timer' and 'Sizer' are the most often proposed size-control models, other models have been suggested, including 'Adder' in which a fixed volume is added to a cell or organism during growth (Campos et al., 2014; Taheri-Araghi et al., 2015), and 'Folder' in which the organism increases in volume by a fixed proportion (Towbin and Grosshans, 2021). It is not trivial to determine which

model most accurately describes growth of individual cells or whole organisms because quantitative measurements of growth must be collected at high precision and throughput under tightly controlled experimental conditions. In unicellular organisms, the development of high-throughput experimental techniques in combination with theoretical models have advanced the understanding of size control (Cadart et al., 2018; Jorgensen and Tyers, 2004; Osella et al., 2014; Soifer et al., 2016; Wang et al., 2010). Progress has been slower for multicellular organisms because cell growth within tissues and tissue growth within organisms often progress at different rates, suggesting that they are likely not regulated in the same ways (Moss-Taylor et al., 2019; Spence, 2009; Uppaluri et al., 2016).

The nematode *Caenorhabditis elegans* presents both a scalable and tractable multicellular animal model to study growth control. With an adult body length of approximately 1 mm, hundreds of thousands of individuals are easily cultured in controlled laboratory conditions (Wood, 1988). Moreover, *C. elegans* post-embryonic development is marked by several molts that provide clear developmental milestones (Page and Johnstone, 2007a). Each molt is initiated by a period of inactivity (lethargus) and terminated once the animal successfully sheds its collagen-rich outer cuticle (ecdysis) (Singh and Sulston, 1978). Four molts separate the *C. elegans* life cycle into five distinct stages: four larval stages (L1-L4) and adult. The timing of these molts determines the completion of stage-specific development (Monsalve et al., 2011; Zaidel-Bar et al., 2010) and underscores the importance of growth regulation during *C. elegans* larval development.

A full description of an organism's development includes the assessment of how growth and body size are regulated. Initial studies of *C. elegans* development described whole-organism growth as a sigmoidal curve characterized by continuous larval growth in length that reaches saturation in adulthood (Byerly et al., 1976). These early studies hypothesized that molt events had little effect on continuous growth as the *C. elegans* cuticle allowed for stretch during larval stages. Later work determined that larval progression was not continuous but rather piecewise in nature (Knight et al., 2002). This study showed that *C. elegans* volumetric growth rate increased from stage to stage such that L1 animals had the slowest rate of growth and L4 animals

86 had the fastest. This finding suggests that *C. elegans* have a mechanism for regulating growth rate, potentially

87 at each molt. Next, researchers using single-animal imaging strategies observed that animals did not advance

88 to the next developmental stage until a critical volume was reached (Uppaluri and Brangwynne, 2015). This

89 finding suggests that *C. elegans* growth follows a 'Sizer' model with each molt decision controlled by a volume

90 threshold and further implies that individual cells are able to communicate information about body size to

91 precisely regulate growth. Most recently, live imaging and characterization of body volume heterogeneity

92 revealed that with respect to the start of a larval stage, *C. elegans* volume fold change within a stage is nearly

93 invariant thereby preventing rapid divergence in volume between fast and slow growing animals (Towbin and

94 Grosshans, 2021).

95 Extensive characterization of *C. elegans* body size mutants has revealed several processes that influence

96 growth rate and body size (Tuck, 2014). A number of genes act through signaling pathways to influence growth

97 and body size (McKeown et al., 1998; Patterson and Padgett, 2000). Some of these pathways contribute to

98 body size control by regulating cuticle collagen genes (Madaan et al., 2018). Alternatively, mutations in some

99 cuticle collagen genes directly disrupt the physical structure of the cuticle (Page and Johnstone, 2007b). These

100 structural changes act as physical constraints on growth as opposed to regulatory mechanisms of growth

101 control. Environmental factors also play a significant role in *C. elegans* growth control. Food restriction is

102 known to decrease growth rate or, when extreme, induce complete developmental arrest (Baugh, 2013; Hu,

103 2018; Uppaluri and Brangwynne, 2015). In *C. elegans*, mutations that disrupt the ability to properly consume

104 food also cause individuals to be small and thin, indicating that food intake can act as a physical constraint on

105 growth and body shape (Mörck and Pilon, 2006).

106 To understand *C. elegans* growth control at the whole-organism level, precise measurements of body size and

107 shape for large numbers of individuals are required. Using a combination of quantitative growth measurements

108 and mathematical modeling, we performed a high-resolution longitudinal study of *C. elegans* larval progression

109 and captured high-precision details about animal length, width, volume, and feeding dynamics. By investigating

110 *C. elegans* feeding and growth in tandem for thousands of individual animals, we found decreases in feeding

111 behavior associated with each larval transition that were also correlated in time with changes in growth. We

112 used our large-scale measurements of body size to further analyze the periods of time surrounding each larval

113 transition. At each molt, we observed simultaneous increases in length, decreases in width, and maintenance

114 of volume, suggesting that body shape in addition to size plays a role in the control of *C. elegans* growth.

115 Given these data, we propose a "Stretcher" mechanism for growth control whereby *C. elegans* senses body

116 size through physical constraints on cuticle stretch and undergoes larval-stage transitions when the cuticle

117 reaches its maximum capacity for stretch. Additionally, we propose that *C. elegans* are able to physically

118 constrain growth rate by modulating food intake. We used quantitative models of eating and growth to evaluate

119 our data and predicted that the rate of volumetric growth is controlled by animal feeding rate and metabolic

120 regulation. Food allocated toward growth reached maxima and minima at larval transitions, indicating

121 increased metabolic control at these points in development.

122 **Results**

123 **Quantitative measurements of *C. elegans* growth**

124 We have optimized a quantitative growth assay that reliably measures small changes in *C. elegans* body size

125 throughout development (Fig 1). Our method provides both high-throughput and high-precision assessment of

126 developmental growth. In brief, populations of 100,000 animals were cultured in flasks. We cultured six

127 replicate populations of *C. elegans* for a total of 600,000 synchronized and growing animals. Every hour after

128 feeding, a sample of the population from each flask (~300 animals/flask) was collected to measure animal

129 length, width, and feeding rate. Feeding rate, examined using fluorescent microspheres, and body size were

130 measured using the COPAS BIOSORT (Union Biometrica). Then, the ImageXpress system (Molecular

131 Devices) was used to collect images of sampled animals. This platform allowed for the further analysis of life

132 stage and body size, contributing added precision to our measurements.
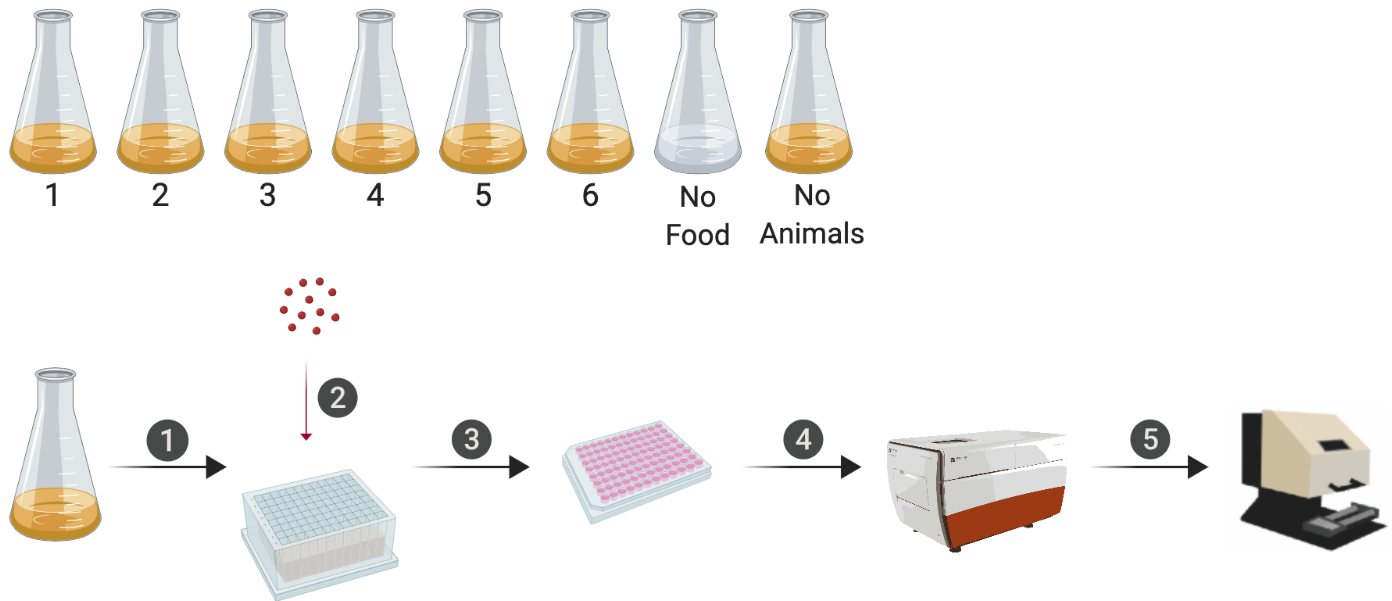
Fig 1. An overview of the quantitative growth assay.
Schematic of the experimental workflow was created with BioRender.com. Synchronized animals were cultured in flasks where six flasks contained replicate populations of nematodes, one flask had a population of unfed animals, and one flask only contained bacterial food. At each hour of the experiment, all eight flasks were sampled. In step 1, animals were transferred from each flask to a single well of a 96-well microtiter plate. In step 2, fluorescent beads were added to each well. Following a 10-minute incubation period, animals from each well of the deep-well plate were transferred to several wells of a 96-well microtiter plate for step 3. In step 4, animals in each well of the microtiter plate were imaged. In step 5, the same animals were measured using the COPAS BIOSORT. This process was repeated every hour after feeding for 72 consecutive hours (see Methods).

The raw data from the quantitative growth assay provides measurements of body size and feeding behavior, which are traits related to animal growth. Two measurements of body size were collected from raw data taken from the COPAS BIOSORT: time of flight (TOF) and optical extinction (EXT) (S1 Fig). Time of flight is a measurement of body length, and optical extinction corresponds to optical density, a measurement influenced by body length, thickness, and composition (Andersen et al., 2015; Pulak, 2006). We investigated whether optical extinction could be correlated to a different measure of body size using the collection of manual size measurements from images (see Methods). We calculated the median length, width, area, and volume of animals in a subset of imaged wells from each hour of the experiment. We then compared these values to well median statistics from the processed COPAS BIOSORT data. We found a strong correlation between manual measurements of animal length from the image analysis and TOF measurements from the COPAS BIOSORT

7

153 (S2 Fig). We also observed an equally strong correlation between manual measurements of animal area and

154 EXT as well as animal width and EXT normalized by body length (norm.EXT). We then approximated animal

155 volume using measurements from the COPAS BIOSORT by using a cylindrical approximation for *C. elegans*

156 shape (see Methods). This result expanded the number of body size parameters that we were able to assess

157 using the COPAS BIOSORT data, allowing us to investigate growth dynamics in length, width, and volume (Fig

158 2A-C). To disentangle nematode objects from non-animal objects (bacteria clumps, detritus, shed cuticles), we

159 employed model-based clustering to remove unwanted objects and better examine growth of animals (S3 Fig).

160 Lastly, we converted COPAS BIOSORT measurements into microns (see Methods).
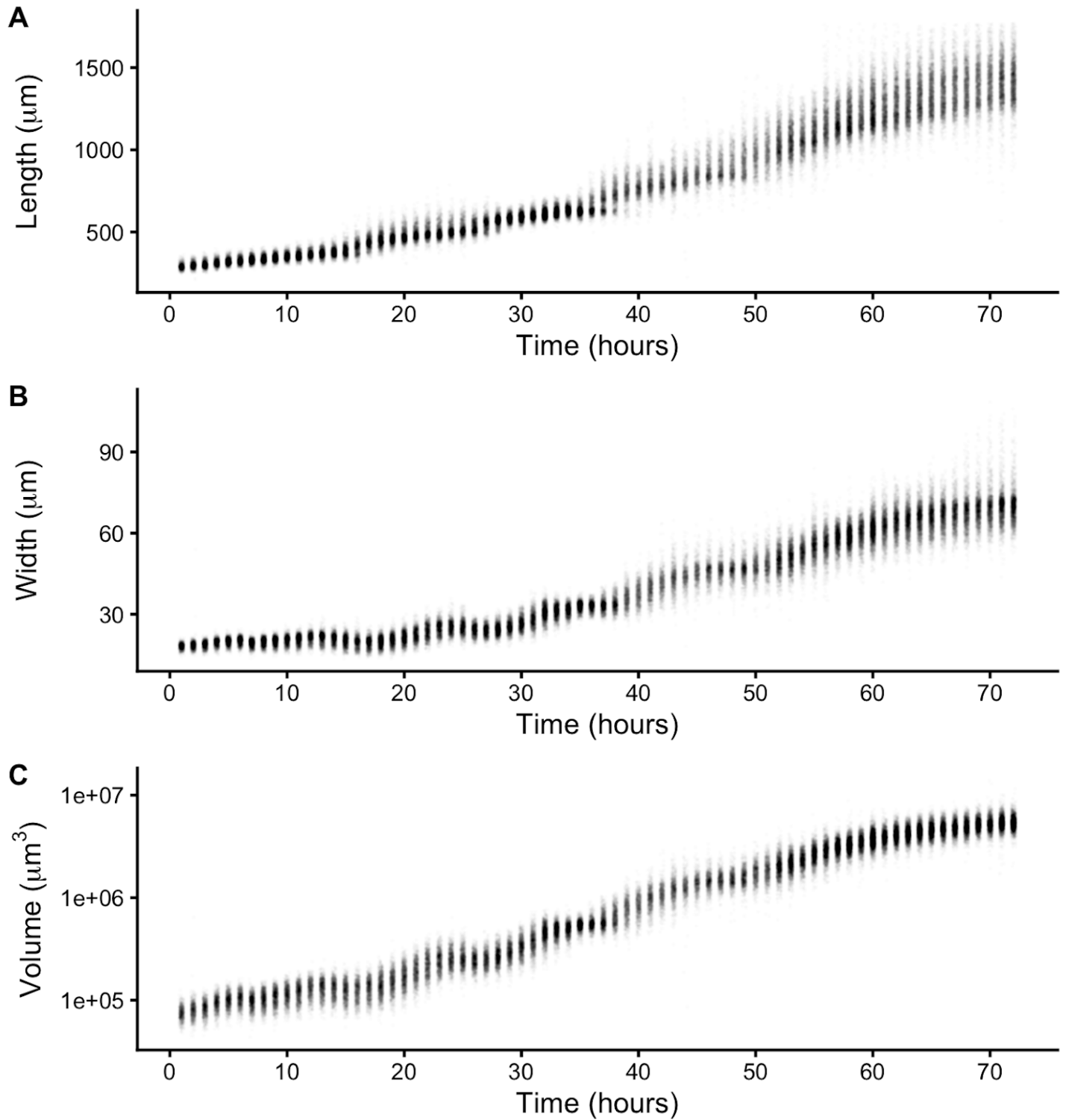
Fig 2. Quantitative measurements of animal size.
COPAS BIOSORT data of animal length (A), width (B), and volume (C) after the removal of non-animal objects using model-based clustering methods (see Methods).

9

164 We report body length, width, and volume of animals at each hour of development from L1 to adult (S1 Fig and

165 Fig 2). Historically, growth of *C. elegans* has been shown as a sigmoidal curve where exponential growth

166 during larval stages reaches a maximum rate in adulthood (Byerly et al., 1976). More recently, researchers

167 have identified that growth curves are discontinuous during development punctuated by larval transitions

168 (Knight et al., 2002; Uppaluri and Brangwynne, 2015). Using our quantitative growth assay, we captured these

169 small-scale discontinuities in larval growth as well as an apparent growth maximum during early adulthood. We

170 noticed that all size variables (length, width, and volume) displayed these dynamics. Objects identified as

171 animals appear to grow in size. However, in particular time windows during development, growth dynamics

172 visibly shift, producing discontinuities in animal growth rate. With these data, we were able to further

173 investigate *C. elegans* growth and size control.

Fluorescence provides a quantitative measurement of animal feeding behavior and developmental progression

176 In addition to body size and shape, the raw data from the quantitative growth assay described above measured

177 fluorescence of each animal object. To readily assess the thousands of measurements acquired at each hour,

178 we generated summary statistics of median well measurements (S1 Table). With these summarized data, we

179 investigated the relationship between feeding behavior and developmental stage. It is well established that

180 temporary suspensions of *C. elegans* feeding occur during each molt (Byerly et al., 1976; Cassada and

181 Russell, 1975). As such, active feeding is frequently used to distinguish growing animals from individuals in a

182 molt. We quantified feeding behavior by exposing animals to fluorescent beads the approximate size of

183 bacteria and measuring fluorescence of animals (Nika et al., 2016). Because larger animals are able to

184 consume more food and therefore contain more ingested food, we normalized fluorescence by animal area to

185 account for increases in body size (S4 Fig). The resulting fluorescence data showed a dynamic pattern (Fig

186 3A). At approximately 15 hours, fluorescence steadily increased to a peak before decreasing back to initial

187 levels at approximately hour 27. This pattern, repeated three additional times, established clear time windows

188 of local minimal fluorescence. These local minima represent periods of time where a large proportion of the

10

189 population had reduced or ceased feeding and therefore suggests time windows where a majority of animals

190 were likely not feeding because they were in a molt. We used a local kernel regression method to estimate a

191 smooth curve and calculate the derivative to identify the time associated with each local minimum (see

192 Methods). We then assessed images collected from the growth assay and demonstrated that periods of

193 decreased feeding are concurrent with the presence of shed cuticles, supporting that animals are undergoing a

194 molt during these periods of time (S5 Fig). When we overlaid the timing of each local minimum on the

195 population size data, we were able to outline the start and end of each larval stage (Fig 3B-D). Notably, local

196 minima occurred approximately every ten hours, consistent with well established observations of molt timing

197 (Byerly et al., 1976). Furthermore, we observed a clear relationship between changes in feeding behavior and

198 growth dynamics where decreases in feeding occurred simultaneously with discontinuous growth in length,

199 width, and volume.
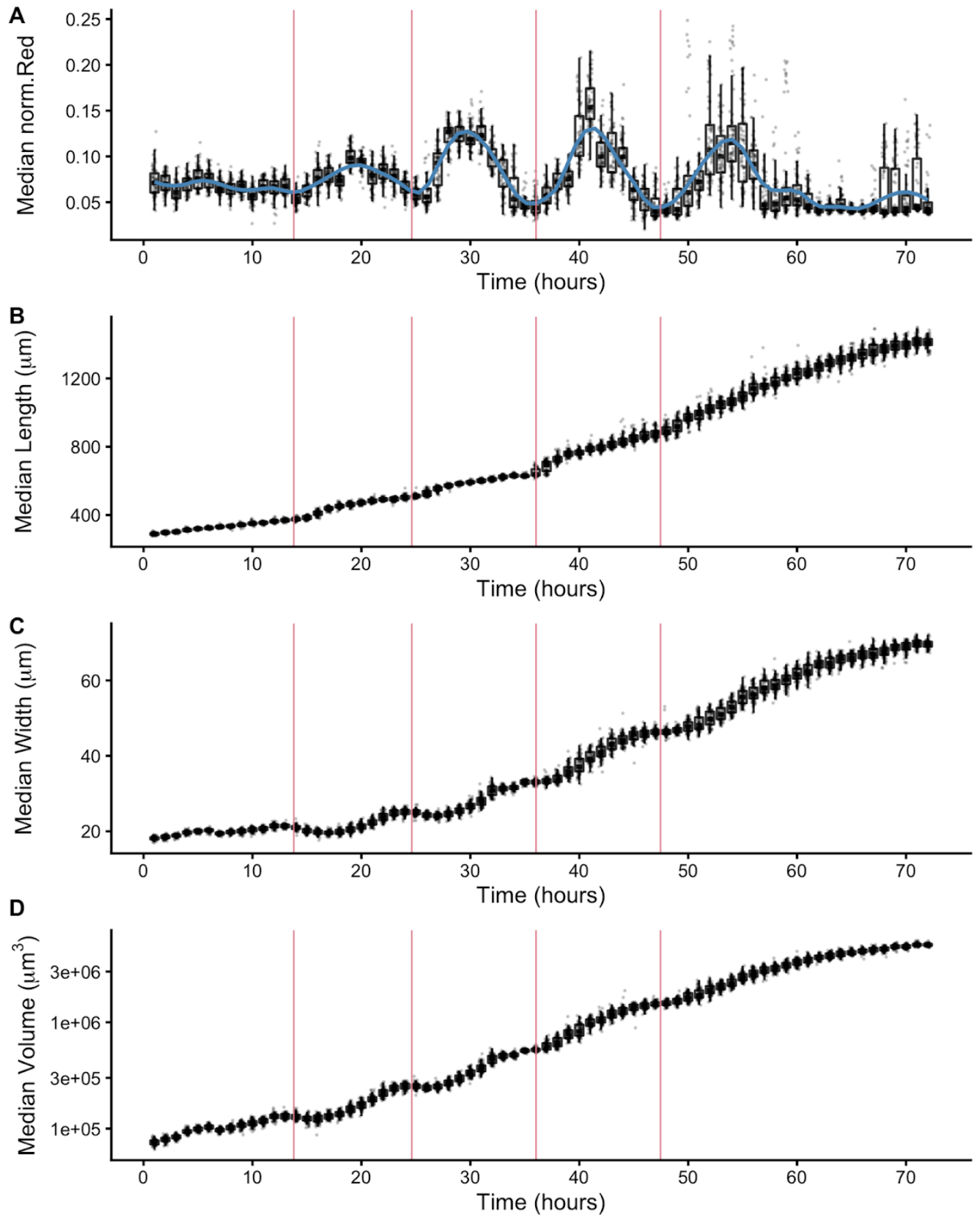
Fig 3. Fluorescence dynamics outline larval stages.

(A) Median normalized red fluorescence (y-axis) over time (x-axis) is shown. The blue line represents the kernel regression fit to the data. The red vertical lines correspond to the local minima of the regression and represent the transition between larval stages. Median length (B), median width (C), and median log volume (D) are shown with larval-stage transitions as well. Upper and lower bounds of the box plots correspond to the first and third quartiles. The upper and lower whiskers extend to 1.5 times the value of the interquartile range.

Changes in *C. elegans* body shape occur at larval-stage transitions

Adult body size is ultimately determined by the coordination of developmental progression and rate of growth. To understand how *C. elegans* achieve final size, we must first examine how *C. elegans* grow. Quantitative studies of *C. elegans* growth frequently assess changes in length or volume over time; however, to fully characterize changes associated with growth, it is also important to consider the dynamics of width. Two general models were proposed for *C. elegans* growth in volume: linear and exponential (Byerly et al., 1976; Knight et al., 2002; Uppaluri and Brangwynne, 2015). Notably, these volume growth models require different dynamics in length and width. To achieve linear volume growth, length and width must increase at precise sublinear rates that together result in a linear increase in volume. If animal length and width increased at a constant linear rate, then volume would increase at a cubic rate. Alternatively, if both length and width grew exponentially, then volume would fit an exponential model. We sought to identify which model best described *C. elegans* growth behavior but were unable to consistently distinguish between linear, exponential, and cubic models using statistical information criterion because of the similarity in the shapes of the growth curves (S6 Fig and S2 Table). This result is not surprising because computational simulations have shown that increases in experimental noise, above 2% added noise, limit the correct identification of growth models (Vuaridel-Thurre et al., 2020).

Growth has important implications for how animals regulate size. Size homeostasis requires that growth rate and developmental rate are coordinated. *C. elegans* reach a similar volume at each larval transition despite significant variation in individual growth rates (Uppaluri and Brangwynne, 2015). Because individuals in a population maintain similar sizes despite differences in growth rate, a control mechanism to regulate developmental progression must exist. Early work proposed a size-based growth control model in *C. elegans*

13

227 *(Uppaluri and Brangwynne, 2015)*, while recent work suggests that size homeostasis is achieved through a

228 folder mechanism where growth rate and development are coupled (Towbin and Grosshans, 2021). To assess

229 changes in body size and shape during a larval transition, we examined the dynamics of animal length, width,

230 and volume in the hours before, during, and after each molt. We find that for each shape variable, larger

231 animals enter molt first (Fig 4). We also observe differences in the distributions of lengths during a larval

232 transition compared to widths and volumes. Measurements of animal width and volume remain unimodal

233 throughout a molt, but length does not. As larger animals begin to exit the molt, an increase in body length

234 occurs that leads to the appearance of bimodality of lengths across the population. This length increase occurs

235 simultaneously with a decrease in widths across the population. Importantly, volume remains constant while

236 length increases and width decreases, indicating a change in body geometry not size (Fig 3 and Fig 4). These

237 changes in the physical dimensions at each larval transition suggests that body shape, in addition to size, is

238 involved in the control of *C. elegans* growth.
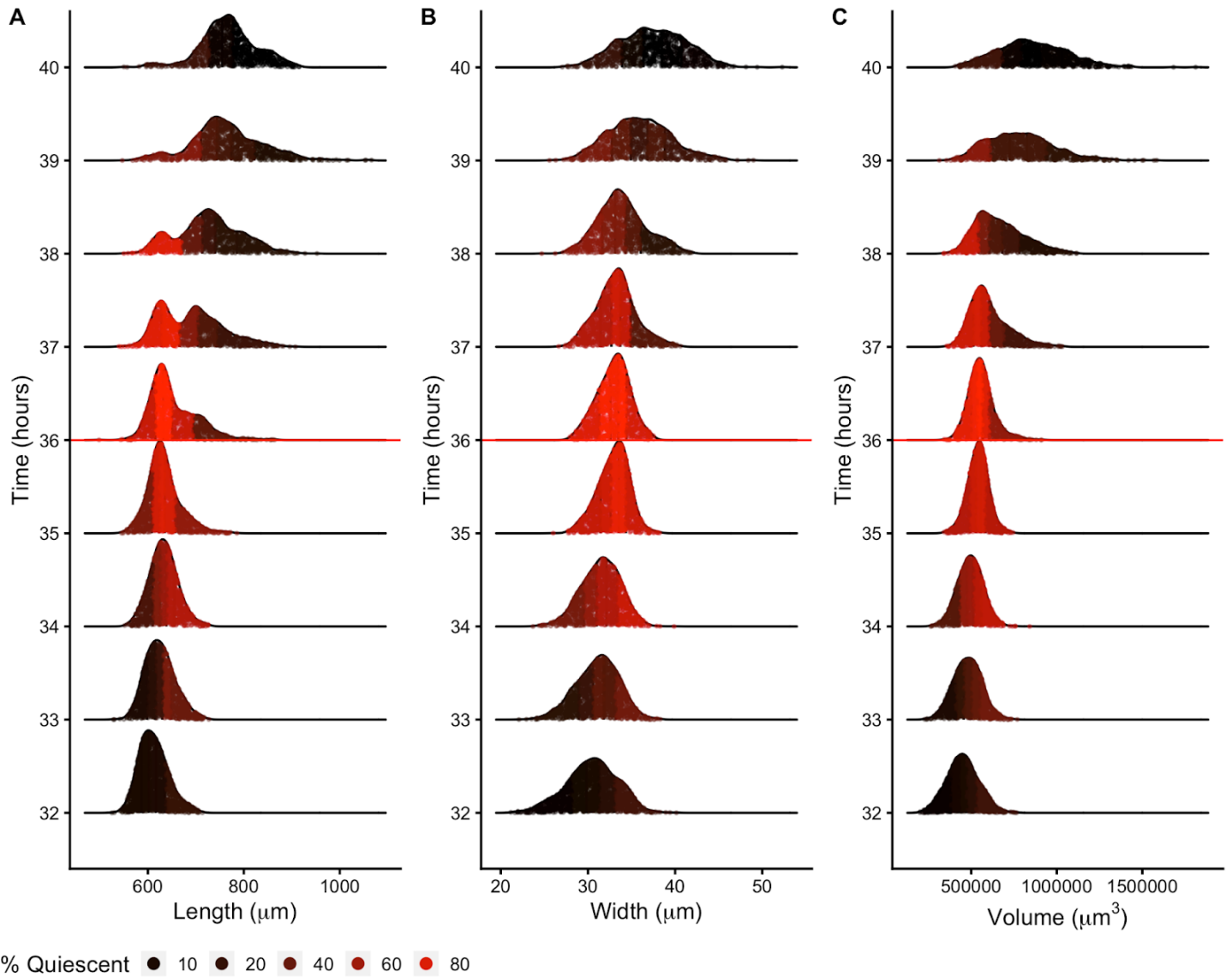
Fig 4. Density plots of population size dynamics during a single larval transition.
Population density curves of length (A), width (B) and volume (C) for the hours surrounding the L3 - L4 larval transition (red horizontal line at 36 hours corresponds to the molt). Each distribution was divided into five quantiles. The percentage of quiescent animals present within each quantile was calculated (see Methods), and each quantile was colored to reflect this percentage. In all shape variables, quantiles that contain the largest animals displayed an increase in quiescence earlier than quantiles that contain the smallest animals. These dynamics were consistent across all larval-stage transitions (S7 Fig).

Measurements of body shape suggest that cuticle stretch determines the timing of larval-stage transitions

Previous studies theorized that the internal mechanism for sensing body size and triggering molts in *C. elegans* is driven, in part, by the properties of the collagen-rich cuticle (Towbin and Grosshans, 2021; Uppaluri

15

250 and Brangwynne, 2015). Many cuticle collagen mutations cause morphological defects in nematode shape

251 some of which cause animals to be shorter but do not impact animal width, implying that the cuticle affects

252 length and width independently (Brenner, 1974). The *C. elegans* cuticle does not grow through the addition of

253 new material, but rather stretches to accommodate increases in animal body size. Cuticle stretch is likely

254 limited by the material properties of the cuticle. The *C. elegans* cuticle is primarily made of cross-linked

255 collagens organized into lateral ridges and circumferential bands (Page and Johnstone, 2007b). Commonly

256 found in many biological systems, collagen-based materials are fairly flexible under low stress conditions.

257 However, as stress increases, collagen fibrils may become elongated and orient in the load bearing direction

258 leading to a decrease in elasticity (Holzapfel, 2017). Previous work using atomic force microscopy revealed a

259 high level of biomechanical stiffness at the circumferential bands (Essmann et al., 2017), leading others to

260 speculate that mechanical strain on these structures is likely adjusted as internal body pressure changes

261 (Dodd et al., 2018). Additionally, in *nekl-3(sv3)* molting mutants, the cuticle is not properly removed from the

262 middle part of their body, leaving the free head and tail to grow normally while the encased middle is

263 constricted by the old cuticle to pre-molt dimensions (Yochem et al., 2015). Given this body restriction, we

264 speculate that the old cuticle stretches beyond its tolerance, becomes stiff, and constricts the center of the

265 nematode relative to the growing head and tail size. We hypothesize that *C. elegans* sense when the cuticle

266 becomes restrictive and use a threshold in the reduction of elasticity or "stretchiness" of the cuticle to

267 determine when to initiate a molt.

268 To explain the initialization of molt behavior, we developed a "Stretcher" model for a cuticle-stretch-based

269 threshold that triggers *C. elegans* larval-stage transitions. We propose that the nematode passes through three

270 distinct regimes related to cuticle stretch: linear stretch dynamics, non-linear stretch dynamics, and larval stage

271 transition (Fig 5). The cuticle structure is anisotropic, possibly leading to distinct properties in the length and

272 width directions (Cox et al., 1981; Petzold et al., 2011). We approximated the cuticle as a hollow cylinder of

273 negligible thickness filled by the body of the nematode. Growth was modelled as internal pressure evenly

16

274 applied to the cuticle in all directions. We hypothesized that the cuticle responds differently during linear

275 stretch, nonlinear stretch, and post-molt relaxation.
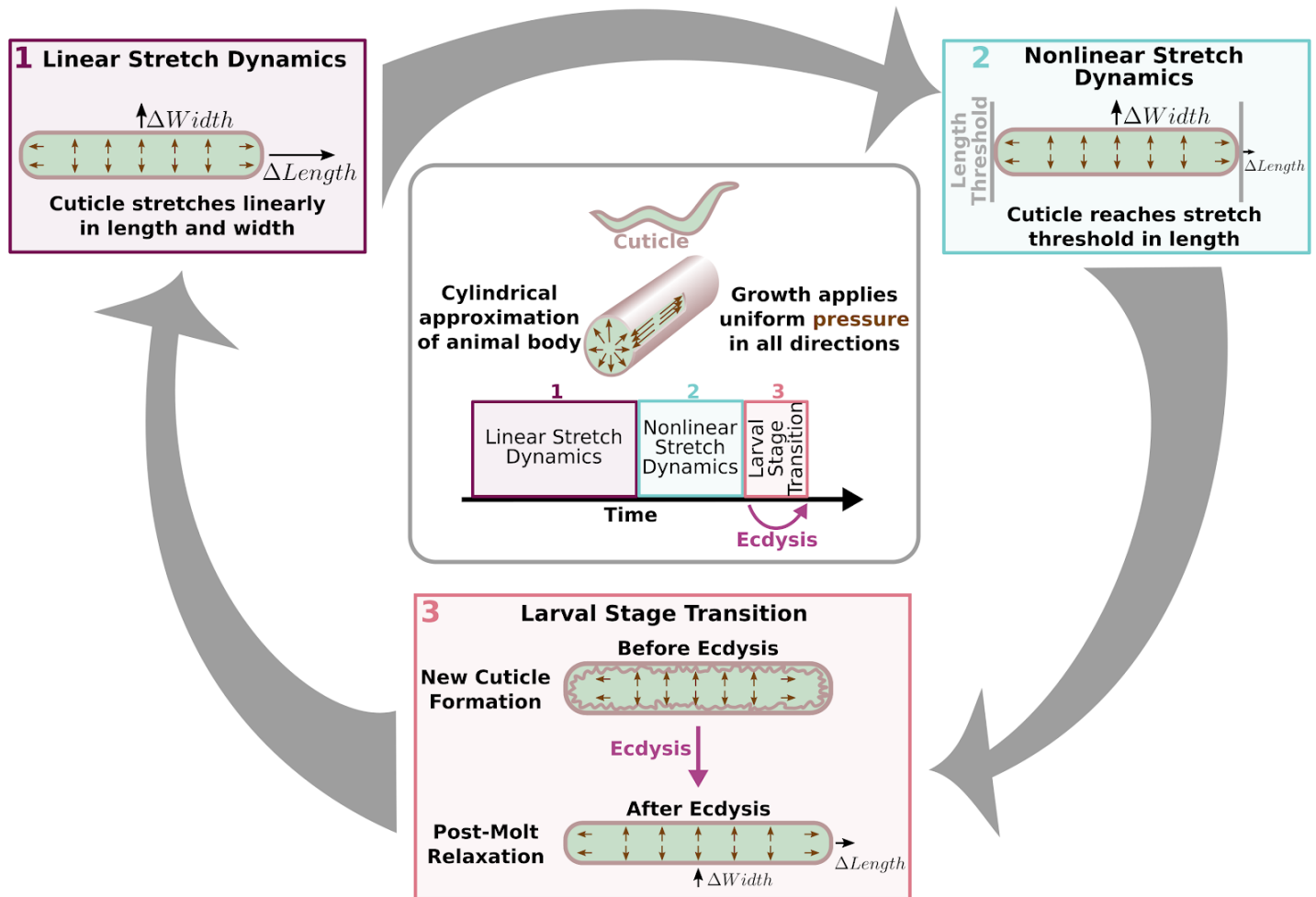
Fig 5. Cuticle stretch determines larval-stage transitions
The "Stretcher" model describes each larval stage as a cycle. Nematodes are modeled as a cylindrical object with a thin cuticle epidermis. (Box 1) Linear Stretch Dynamics: uniform growth pressure stretches the cuticle linearly in both length and width. (Box 2) Nonlinear Stretch Dynamics: the cuticle has reached a stretch threshold in length, and under uniform growth pressure the length stretches less (sub-linear) and width stretches linearly. (Box 3) Larval Stage Transition: a new cuticle is formed and the old cuticle is shed (ecdysis), removing constraints in length. The nematode body "relaxes" in length, causing an increase in length, a decrease in width, and constant volume.

284 In the linear stretch regime (Fig 5), the cuticle would be linearly elastic in both the length and width directions,

285 stretching proportionally to the pressure exerted on the cuticle. Previous work found evidence for a linearly

17

286 elastic cuticle (Gilpin et al., 2015; Park et al., 2007) in animals expanded in a negative external pressure

287 environment or after positive force was applied to the cuticle. Gilpin *et al.* have found evidence of linear

288 elasticity in the nematode body. We conjecture that this linear elasticity is caused by the constraints applied by

289 the cuticle ((Gilpin et al., 2015; Park et al., 2007). A linearly elastic cuticle will have ΔL stretch in the length

290 direction and ΔW stretch in the width direction, each related to growth-applied pressure Δp by

$$\Delta L = a_L \Delta p \tag{1}$$

$$\Delta W = a_W \Delta p. \tag{2}$$

293 The "stretch coefficients" in length, a_L, and width, a_W, measure the stiffness of the cuticle (S5 File, Eq.

294 S14-S23). Smaller values correspond to a stiffer material, which is less able to stretch in response to pressure.

295 The stretch coefficients are constant in the linearly elastic regime and are determined by geometric constants

296 and material properties. The ratio of the change in length (Eq. 1) and width (Eq. 2) produces a

297 pressure-independent relationship that depends only on the ratio of the geometric and material properties,

298 which can be verified using measurements of length and width (Fig. 3). During the linearly elastic regime, the

299 ratio of growth in width to growth in length is constant throughout a larval stage where the cuticle properties are

300 fixed as in

$$\frac{\Delta W}{\Delta L} = \frac{a_W}{a_L} = constant. \tag{3}$$

302 In the non-linear stretch regime (Fig 5), growth continues to apply pressure to the cuticle uniformly in all

303 directions. As observed in *nekl-3(sv3)* mutants, the cuticle can restrict body growth (Yochem et al., 2015).

304 Once outside of the linearly elastic regime, the cuticle would hardly stretch, even under large forces. We

305 hypothesized that this shift from linear to nonlinear regimes provides a mechanism for size-sensing and cues

306 the larval-stage transition (Fig 5). In principle, this transition could occur in either the width or length directions.

307 For ease of presentation, we assume a transition from linear to non-linear stretch in the length direction and

18

308 maintains linear stretch in the width direction. In the nonlinear regime, the stretch in the length direction in

309 response to pressure becomes

310
$$\Delta L \approx \tilde{a}_L(p)\,\Delta p. \tag{4}$$

311 The nonlinear "stretch coefficient," $\tilde{a}_L(p)$, is no longer constant and decreases with increasing pressure. It is

312 smaller than a_L because the cuticle has become less elastic than in the linear regime. If the length-direction

313 enters the nonlinear regime and has reduced stretch response, while width has the same constant stretch

314 response then, we expect the $\frac{\Delta W}{\Delta L}$ ratio to increase

315
$$\left.\frac{\Delta W}{\Delta L}\right|_{non-linear} = \frac{a_W}{\tilde{a}_L(p)} > \frac{a_W}{a_L} = \left.\frac{\Delta W}{\Delta L}\right|_{linear}. \tag{5}$$

316 During the larval-stage transition (Fig 5), a new, larger cuticle is formed beneath the old cuticle that is shed

317 during ecdysis. Because the old cuticle constrained growth in length, we predict a rapid increase in the length

318 direction when the constraint is removed. Nematode volume is conserved as growth does not occur during this

319 process. Therefore, the relaxation in length is accompanied by a corresponding decrease in width.

19
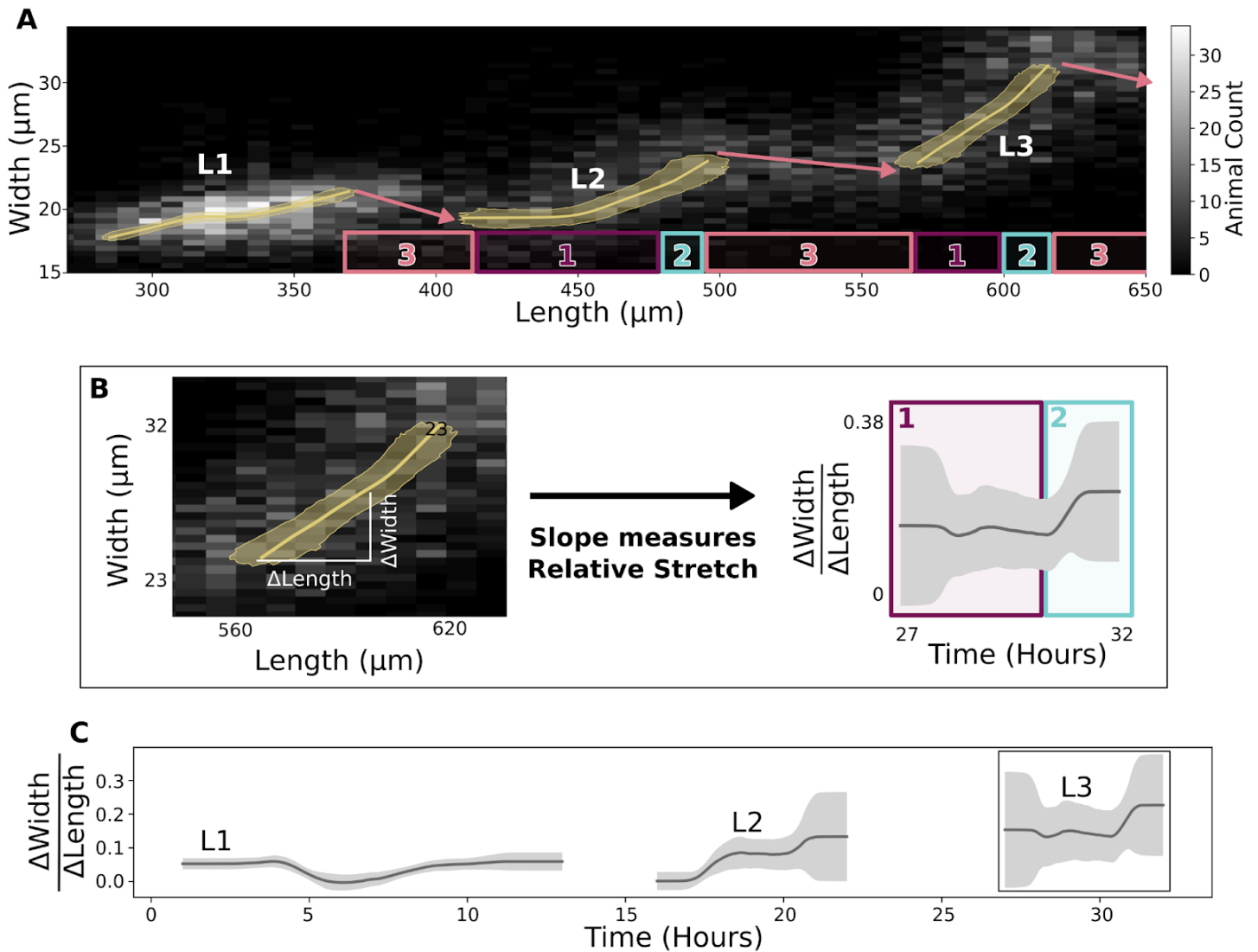
Fig 6. Stretcher model analysis of replicate 2 COPAS BIOSORT data consistent with a length trigger for molting

(A) A grayscale histogram of the width (y-axis) vs length (x-axis) of all sampled animals in replicate 2. The range of all bootstrap regressions is in gold. (B) Demonstration of calculating the ratio of width-to-length stretch as the local slope using L3. Left panel is a repetition of L3 data from Fig 6A. Right panel is a repetition of results from Fig 6C. (C) Within a larval stage, the ratio of width to length stretch varies over time. The standard deviation captures population variation (grey) (S5 File, Eq. S26, S28).

To verify the shape dynamics predicted by the Stretcher model, we analyzed the relationship between nematode length and width over developmental time. All three regimes, linear stretch, non-linear stretch, and relaxation, predicted by the Stretcher model are detectable in the COPAS BIOSORT data (Fig 6). In all larval stages, the instantaneous ratio $\frac{\Delta W}{\Delta L}$ was approximately constant for the majority of the time, consistent with a linear stretch regime (Fig 6C). We observed a large slope decrease during the L1 stage, which could

20

332 correspond in time to the metabolic decision for entry into the dauer stage (Golden and Riddle, 1984) or

333 divisions of the seam cells (Sulston and Horvitz, 1977). Near the end of L2 and L3 stages, we observed a

334 sharp slope increase, supporting our predictions of a non-linear stretch regime in length prior to lethargus.

335 Slope transitions are difficult to detect at all larval stages due to noise amplification present in slope

336 calculations and population effects, making the larval stage boundaries difficult to define in a consistent

337 manner. We note that the transitions between larval stages contain the expected increase in length and a

338 decrease in width (Fig 6A and S8 Fig) consistent with a length threshold in the Stretcher model. Though the

339 shape relaxation for an individual animal is expected to happen at a much shorter time scale than data

340 collection (seconds to minutes), the measured shape change within the population occurs on a larger time

341 scale of several hours. As different individuals reach the transition points at different times, the shape change

342 is smoothed out and difficult to observe in the time-course data (Fig 3). However, we were able to more readily

343 observe the sudden shape change at transitions by looking at the width and length because animals of similar

344 shape are grouped together, regardless of the time they were observed (Fig 6A). These results suggest that

345 the material properties of the cuticle could generate a mechanical signal for the start of larval transition.

346 Additionally, sensing when the cuticle reaches a critical stiffness would allow the animal to detect when a

347 certain fold change occurs.

348 **Mechanical control of feeding and allocation of food energy likely constrain growth dynamics**

349 We have shown that changes in physical properties of the *C. elegans* cuticle precede the decision to initiate

350 molt and might serve as a cue for developmental timing. *C. elegans* must have mechanisms to control growth

351 throughout development, particularly in response to these cues. Like most species, *C. elegans* do not increase

352 their growth rate indefinitely in response to increased food availability (Uppaluri and Brangwynne, 2015). The

353 animals could control growth entirely using feeding rate, as they actively control the feeding rate (Fang-Yen et

354 al., 2009) and stop feeding at the initiation of a molt (Singh and Sulston, 1978). In addition to this mechanical

355 control, they could use metabolic control to preemptively divert ingested resources toward or away from

356 growth. Metabolic processing of stored resources could be especially useful if animals complete their molt and

357 enter a food-limited environment. For these reasons, we investigated the possible mechanical control of

358 feeding (Fig 7) and the metabolic control of the allocation of ingested food toward organismal growth and

359 development (Fig 8). Using a quantitative feeding model, we calculated the rate of mechanical feeding

360 behavior from animal volume and food intake data. Additionally, we calculated an estimate for allocation of

361 ingested food toward volumetric growth.
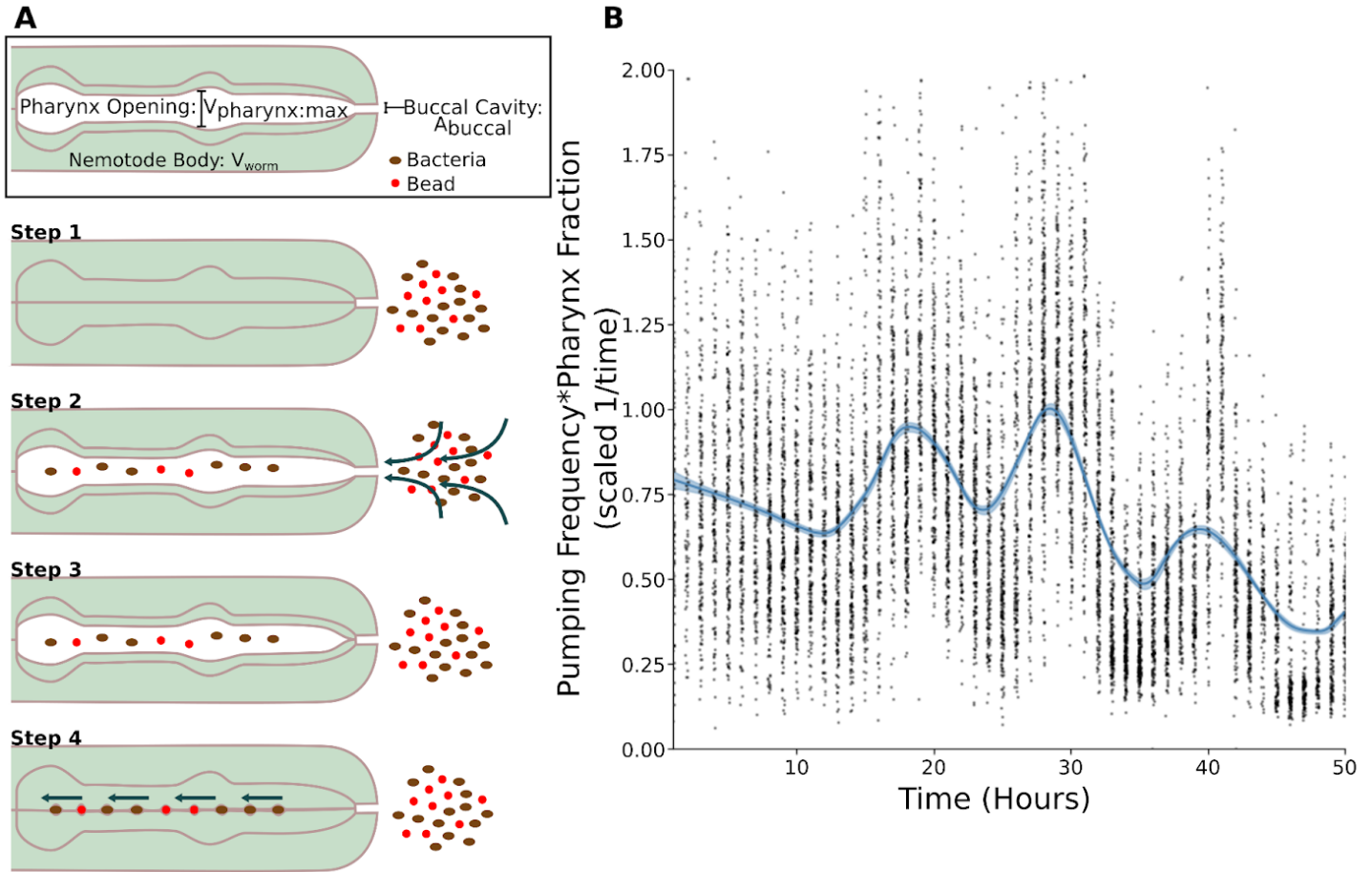
362 **Fig 7. Visualization and analysis of Feeding Model**
363 Schematics for food intake and utilization models are shown. (A) The buccal cavity is the opening through
364 which food enters. The pharyngeal lumen is the cavity opened and closed by pharyngeal muscles that drives
365 food intake. (B) Product of pumping frequency and pharyngeal lumen fraction, $f(t)g(t)$.

22
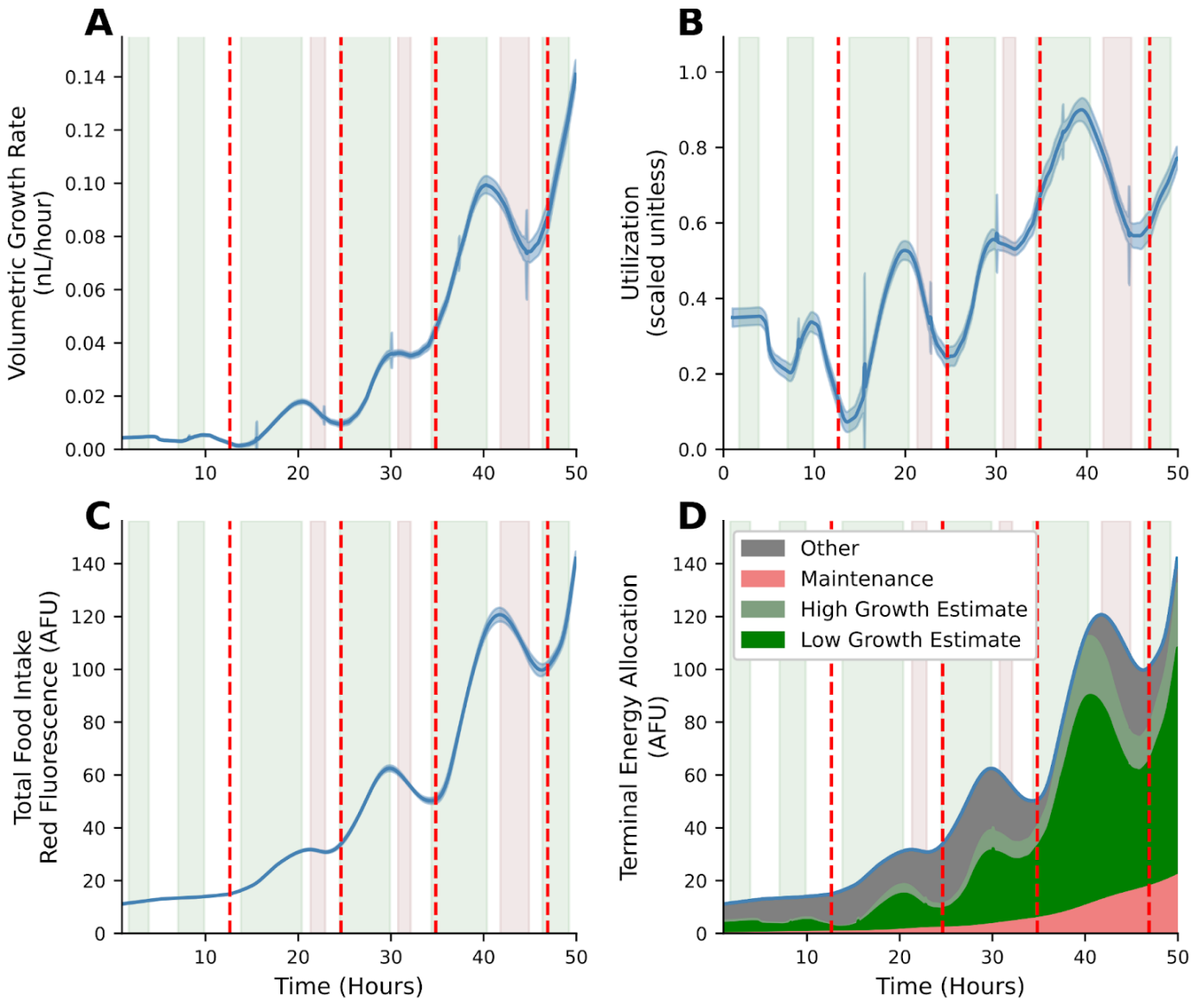
Fig 8. Visualization and analysis of Food Utilization model.
(A) Dynamics of volume growth rate. (B) Dynamics of the estimated food utilization towards growth ($\alpha(t)$). (C) Dynamics of red fluorescence. (D) Dynamics of food allocation breakdown. Food allocated toward maintenance is proportional to animal size (pink). Food allocated toward growth is calculated from food intake (B) and utilization (C) to produce low (dark green) and high (combined green) estimates (S5 File). Food allocated to other metabolic processes consists of remaining food resources (grey). In panels A-C, the solid blue line represents the mean bootstrap regression. Standard deviation on the regression is marked by the shaded blue region. In panels A-D, Vertical red lines mark molt times. Green regions correspond to times during which volumetric growth rate and red fluorescence are both increasing, red regions correspond to times during which volumetric growth rate and red fluorescence are both decreasing, and white regions correspond to times during which volumetric growth rate and red fluorescence do not vary together. Errors on shaded regions are ±0.7 hours. These data are from replicate 2 and are representative of all replicates (S11 Fig).

23

378 Variation in pumping rate controls food uptake

379 *C. elegans* is a filter feeder that pumps its food through a cycle of pharyngeal muscle contractions and

380 relaxations that alternatively open and close the pharyngeal cavity. *C. elegans* are capable of actively

381 modulating the length of time used to contract or open a subset of the pharyngeal muscles (Fang-Yen et al.,

382 2009). Our feeding model describes how control of this time length and thus the control of the overall pumping

383 period, defined as the length of time of one full pumping cycle, translates to changes in the rate of food uptake.

384 A single cycle in which animals take up and transport food to the gut consists of four general steps (Fig 7A).

385 The cycle begins with relaxed pharyngeal muscles and a closed pharyngeal lumen (step 1). The animal opens

386 the pharyngeal lumen so that fluid and food flow through the buccal cavity and into the pharyngeal lumen (step

387 2). The animal cannot create a vacuum, so the volume of the cavity produced must be filled entirely by media

388 and bacteria at the same concentration as the external environment. The animal relaxes the muscles that

389 control the opening, stopping the flow of fluid through the buccal cavity and trapping a volume of media

390 approximately equal to the maximum volume of the pharyngeal lumen (step 3). Finally, the pharynx closes,

391 extruding excess media and trapping bacteria and beads that are then 'swallowed' (step 4). The period of a

392 single cycle varies throughout the life cycle of *C. elegans* (Fang-Yen et al., 2009).

393 We find a relationship between eating rate and animal volume. It has previously been suggested that the

394 cross-sectional area of the buccal cavity is a limiting factor in the rate of food intake (Knight et al., 2002).

395 However, the volume of the pharyngeal lumen is filled with media each cycle, so the volume of the pharyngeal

396 lumen, not the cross-sectional area, sets food uptake rate. We express the volume of the pharyngeal lumen as

397 a fraction, $g(t)$, of nematode volume, $V_{lumen:max}(t) = g(t) \cdot V_{worm}(t)$. As the pumping period is much faster

398 (roughly 200 ms in adults) (Fang-Yen et al., 2009) than the rate of measured growth (hours), we averaged the

399 food intake rate, $\frac{dV_{food}}{dt}$, over a single pumping period (S5 File, Eq. S1-S6) to obtain

$$\frac{dV_{food}}{dt} = Cf(t)g(t)V_{worm} . \tag{6}$$

401 Here, C is the concentration of bacteria in the culture where animals are grown and $f(t)$ is the pumping

402 frequency and the inverse of the period of a single pump. Both pumping frequency, $f(t)$, and the fractional

403 pharyngeal lumen size, $g(t)$, vary over the animal's life cycle. Though any individual bacterium may take

404 multiple pumps to travel down to the gut, we assume that, once food has entered the pharyngeal lumen, it will

405 eventually be metabolized. With this assumption, we are only interested in the rate at which food enters so we

406 do not model the dynamics of food traveling through the gut.

407 We verify that red fluorescence (denoted as "Red") can be treated as a proxy measurement for food intake rate

408 given defecation rates (S9 Fig, S5 File). We use red fluorescence and calculated volume as the product of

409 pumping rate and pharyngeal lumen fraction, $f(t)g(t) \propto \frac{Red}{V_{worm}}$, over time. The product oscillated within a larval

410 stage and decreased across larval stages (Fig 7B). The minima of the product of pumping frequency and

411 pharyngeal lumen fraction occurred during molt times, consistent with prior knowledge (Byerly et al., 1976;

412 Singh and Sulston, 1978). The relative length of the pharynx to animal length has been shown to decrease

413 over development (Avery, 2003) and a similar trend in the volume of the pharyngeal lumen could explain the

414 slow decrease in the product of pumping frequency and pharynx fraction.

415 **Changes in food utilization coincide with molts**

416 To understand whether animals control growth rate primarily using the mechanical feeding process or

417 metabolic regulation, we describe how food is utilized once it is ingested by *C. elegans*. We assumed three

418 general categories of food utilization: maintenance, observed volumetric growth, and all other processes. We

419 assume that resources required for maintenance are proportional to the volume of the animal. Other processes

420 may include the development of tissues and structures, such as reproductive components, within the worm

421 which are resource intensive, but are not detected during the measurements of the width, length, or volume.

422 The rate of food conversion to growth can be described by:

423
$$\frac{dV_{worm}}{dt}(t) = \eta(t)\alpha(t)\frac{dV_{food}}{dt}(t). \tag{7}$$

424 Here, $\frac{dV_{food}}{dt}$ is the instantaneous rate of food intake (averaged over a single pump), $\eta(t)$ is the metabolic

425 efficiency of converting food to growth, and $\alpha(t)$ is food utilization, meaning the fraction of food used for

426 volumetric growth as opposed to maintenance or other metabolic processes. If both $\eta(t)$ and $\alpha(t)$ are constant,

427 then Eq. (4) predicts the rate of volumetric growth is directly proportional to the rate of food consumption, which

428 would be equivalent to controlling growth through feeding with no changes in metabolic regulation (through

429 enzyme expression or other direction of flux between pathways). Efficiency captures the maximum efficiency of

430 metabolism, and we assume it does not vary significantly when the food source is constant, $\eta(t) = \eta$.

431 Therefore, utilization captures the dynamics of metabolic regulation. If the fraction of food utilized for growth is

432 not constant, then volumetric growth rate is no longer proportional to food consumption rate and metabolic

433 control must play a role in driving the growth rate.

434 We calculate the value of the product of metabolic efficiency and food utilization, $\alpha(t)\eta$, from the data by

435 manipulating Eq. (7):

436
$$\alpha(t)\eta = \left(\frac{dV_{worm}}{dt}(t)\right)/\left(\frac{dV_{food}}{dt}(t)\right). \tag{8}$$

437 By using the red fluorescence as a proxy for food intake rate in Eq. (8), we can estimate the dynamical

438 behavior up to scaling factors for the metabolic efficiency times food utilization, $\alpha(t)\eta \propto \left(\frac{dV_{worm}}{dt}(t)\right)/Red$ (Fig

439 8B). Because only utilization varies in time, it captures the dynamics of metabolic regulation:

440
$$\alpha(t) \propto \left(\frac{dV_{worm}}{dt}(t)\right)/Red. \tag{9}$$

441 Feeding rate (using red fluorescence as a proxy) and volume growth rate (numerically differentiated from the

442 volume regression) follow similar dynamics throughout much of *C. elegans* development (Fig 8A, Fig 8C). The

443 regressions for volume growth rate and food intake rate (as measured through red fluorescence) demonstrate

444 a greater than 90% correlation when using synchronized populations (through the end of L4). Each larval stage

445 consists of three types of dynamics: steady growth during which food intake and growth rate are both

446 increasing (green), preparation for molt during which food intake and growth rate are both decreasing (red),

447 and transition regions where food intake and growth rate do not vary together (white). To illustrate how the

448 dynamics of food intake rate and growth rate (Fig. 8A, 8C) correspond to the progression within a larval stage,

449 consider the L3 larvae in replicate 2. At hour 24.5, both growth rate and food intake rate increased

450 corresponding to the start of the third larval stage for the population average. Until hour 29.8, the population

451 grew steadily, and food intake and growth rate both increased (green). Between hour 29.8 and 30.8 (white),

452 food intake decreased and growth rate increased, marking a transition from the steady growth (green) to the

453 molt preparation regime (red). Between hours 30.8 and 32.1, the animals prepared to initiate molts, and both

454 the growth rate and food intake rate decreased (red). Between hours 32.1 and 34.4 (white), the animals'

455 growth rate increased once again while the food intake rate continued to decrease corresponding to the end of

456 the molt and start of the L4 larval stage. Similar dynamics occurred in the L2 and L3 larval stages. The L1

457 larval stage followed different dynamics, likely due to the dauer decision or divisions of the seam cells.

458 During steady growth (green) and molt initiation (red), mechanical food intake rate and allocation of food

459 resources towards observable growth have similar dynamics. At transition points (white) the allocation of food

460 resources towards growth, $\alpha(t)$, reaches a local minimum or maximum (Fig 8B). These local extrema in $\alpha(t)$)

461 at transition points likely indicate large changes in metabolic regulation. One might expect growth rate to lag

462 food intake, but time-lag analysis showed no consistent lag across L1 to L4. During the L1 and L2 stages,

463 volume growth rate lagged behind food intake rate (with correlation ~86%); during the L3 and L4 stages, food

464 intake rate lagged behind growth rate (with correlation ~94%) (S14 Fig). The switch to food intake lagging

465 growth rate at later larval stages might be indicative of increased regulation of resource allocation.

466 One might assume that the high correlation (S15 Fig) between dynamics of growth (Fig. 8A) and food intake

467 (Fig. 8C) imply that animals control their growth rate entirely through the control of mechanical food intake rate

468 with no variation in how food resources are allocated. Instead we saw variation in food allocated toward

469 growth, $\alpha(t)$, both between larval stages and within individual larval stages. We examined the dynamic range

470 of total food intake (Fig. 8C) and the dynamic range of food allocated toward growth (combined green Fig. 8D)

471 to quantify whether control through food intake or control through metabolic regulation play a larger role in

472 growth regulation. Across a larval stage, both methods of regulation had dynamic ranges of the same order of

473 magnitude. We also calculated the dynamic range within each period of steady growth (green), molt initiation

474 (red), and transition (white) (Fig. 8). Within each region, the dynamic range of food intake and food allocated

475 toward growth differed by a factor of 0.5 to 5, but we found no noticeable trends by region (S3 Table). It is

476 possible that the interpolation and smoothing required to calculate derivatives necessary to this analysis are

477 masking some sharper transitions, which could be resolved with higher resolution temporal experiments.

478 These results suggested that both the total intake rate (governed by mechanical feeding behavior) and

479 metabolic regulation of food resources are crucial for growth control in all regions of development. Additionally,

480 we compared the food allocated toward other metabolic processes with food allocated toward growth over the

481 four larval stages. Using the low growth utilization estimate, food allocated toward growth increases with an

482 approximately 86-fold increase while the other resource allocation increases with an approximately six-fold

483 increase. Resource requirements for other metabolic processes such as development of new tissues and

484 animal mobility might vary much less during development than the resource requirements for volumetric

485 growth.

486 Feeding rate and volumetric growth rate share a complex relationship with *C. elegans* development; food

487 intake and growth rate vary together, except at larval stage transitions and possible key developmental

488 transitions. Notably, the changes in metabolic resource allocation at the transition from increasing to

489 decreasing growth and food intake rates (Fig 8A, 8C) occurred at approximately the same times as the

490 increase in slope predicted as a cue for molt initiation by the Stretcher model (Fig 6). This correlation suggests

491 that the cuticle reaches its maximum stretch in length and a metabolic decision to reallocate food resources

492 growth occurs at the same time, supporting the hypothesis that a physical threshold in stretch triggers

493 metabolic decisions to enter a molt (S10 Fig).

28

Discussion

Using an integrated image-based and flow-based phenotyping strategy to precisely evaluate feeding, growth, and molt dynamics at high replication, we detected oscillations in feeding behavior consistent with larval progressions and used these dynamics to define larval stages. We observed changes in body shape at each larval-stage transition that are consistent with differences in physical cuticle properties along length or width (anisotropy). These results suggest that animals sense their size and control molt timing by detecting the physical stretch of the cuticle. To understand whether *C. elegans* control growth using the moderation of the physical uptake of nutrients or through metabolic regulation of the allocation of consumed resources, we applied mathematical models of feeding-limited growth to our data. We predicted that the volumetric growth rate was controlled by both *C. elegans* feeding rate and other metabolic regulation and provided a modeling framework to decouple the relative effects. These results demonstrate two mechanisms by which physical constraints can influence developmental timing and growth rate.

Cuticle stretch controls the timing of larval-stage transitions

Measurement of both animal length and width allowed us to observe changes in body shape as well as body size. We propose that a stretch threshold along the body length axis acts as a trigger to larval-stage transitions. Importantly, mechanical stretch sensing could also provide organisms a way to couple the rate of growth and development to maintain a constant volume fold change within a larval stage and achieve size homeostasis within a population. In this way, smaller animals would reach a stretch limit at a smaller size as the cuticle would only stretch a percentage of its original size before reaching a threshold. A folder mechanism for *C. elegans* growth has been previously suggested (Towbin and Grosshans, 2021). For cuticle stretch to trigger larval-stage transitions, animals must either have the ability to measure the amount the cuticle has stretched or the stiffness of the cuticle. Across biological systems, cells can respond to the stiffness of their environment using mechanosensitive components (Schiller and Fässler, 2013; Wolfenson et al., 2011), but few examples in tissues or whole-organisms are known. In *C. elegans*, it has been demonstrated that

29

518 hemidesmosomes, which connect the cuticle and the epidermis, are mechanosensitive during embryogenesis

519 (Suman et al., 2019; Zhang et al., 2011). Additionally, dense bodies, which connect the epidermis and muscles,

520 are hypothesized to be mechanosensitive as well (Broday et al., 2007; Costa et al., 1997; Moerman and

521 Williams, 2006; Zaidel-Bar et al., 2010). Changes in cuticle composition, and presumably stiffness, have been

522 shown to also affect well known growth controlling pathways such as the BMP signaling pathway (Madaan et

523 al., 2020). These possible mechanosensitive components could monitor the stiffness of the cuticle and be part

524 of the signaling pathways that regulate larval-stage transitions. Further experiments are required to explicitly

525 test whether these components control larval-stage transitions.

526 Our analysis of width-to-length ratio variation over larval stages provides a first approximation of the timing of

527 larval-stage transition cues and cuticle stretch properties (Fig 8). The sudden increase we observed in the

528 width-to-length ratio suggests a length stretch threshold. Interestingly, when observing the L4 to adult

529 transition, others have detected anisotropic constriction on the transverse (width) axis followed by gradual

530 relaxation driven by rearrangements in cortical actin networks (Katz et al., 2018). Single-worm, high frequency

531 measurements targeting hours surrounding the sudden width-to-length ratio increase, are needed to better

532 resolve cuticle shape dynamics. Higher time resolution would also minimize edge effects (S12 Fig), which likely

533 caused the unpredicted width-to-length ratio increase observed at the start of larval stage L2 (Fig 8C).

534 Measurements of animal length and width provide a total stiffness estimate but do not allow us to distinguish

535 the contributions of cuticle stiffness from other tissues. To investigate cuticle properties, independent of other

536 nematode tissues and organs, experiments must probe the stiffness of free cuticles.

537 **Physical constraints on feeding influence growth dynamics**

538 Our mechanical feeding model defines a relationship between food availability, food intake rate, food utilization,

539 and growth rate. We distinguished between food intake rate and pumping rates by modeling the physical

540 process of feeding. The results of our analysis are consistent with both an oscillation in pumping rates (Singh

541 and Sulston, 1978) and a slow change in pharyngeal lumen size throughout development (Avery, 2003).

542 Previous research suggested that pumping frequencies within a larval stage are constant with sudden

543 transitions between lethargus and pumping (Nika et al., 2016). However, we were unable to resolve sudden

544 transitions because of the continuous smoothing of the kernel regression method used and population effects

545 (Fig 7B). Previous work has shown that growth rate increases with increasing food availability up to a

546 saturation limit (Uppaluri and Brangwynne, 2015). Varying bacterial concentration levels in future experiments

547 would allow us to distinguish whether mechanical control of food intake or metabolic control of food utilization

548 determine the upper bound on growth rate.

549 Our analysis of the relationship between growth rate and food intake rate quantified the interplay of metabolic

550 regulation and mechanical food intake. Mechanical food intake provides the upper bound of available food

551 resources for growth, but metabolic regulation substantially changes how much of this available food is utilized

552 for volumetric growth across development. Local extrema in metabolic regulation dynamics coincide with the

553 start of transition times. Within the L2 and L3 stages we observed a decoupling between growth rate and food

554 intake dynamics (Fig. 8 white region) twice. The first of these time periods corresponds to the times at which

555 the width-to-length ratio drastically changes and the second corresponds to ecdysis (S10 Fig). We estimated

556 that throughout larval stages metabolic resources allocated to non-growth processes varies much less than

557 food resources required for growth and maintenance. The oscillatory behavior of food utilization motivates the

558 need for further metabolomic experiments to probe metabolic regulatory dynamics. Higher time resolution

559 experiments on single animals in future experiments may be able to better resolve the existence of sudden

560 changes in metabolic regulation.

561 In the analysis of both the Stretcher and feeding models, we found that the L1 larval stage has different

562 dynamics than other larval stages. We observed a decrease in growth rate with no associated decrease in

563 feeding rate, corresponding to a mid-stage resource reallocation, that does not occur in any other larval stage,

564 possibly showing the dauer decision (Golden and Riddle, 1984) or the divisions of seam cells. Additionally,

565 within the L1 stage, the relative stretch measured in width and length did not follow the pattern observed in

566 other larval stages. We observed a mid-stage dip in the width-to-length ratio that is otherwise approximately

567 constant throughout the L1 stage. As animals reallocate food resources in mid-L1, they also undergo a change

568 in shape suggesting either directed growth or structural changes to either the cuticle or animal body (Fig 3, Fig

569 6, S8 Fig). Future experiments exploring the structural properties of cuticles at all larval stages may help to

570 determine where the L1 shape changes originate.

571 **Development comprises complex interactions of growth regulation across diverse scales**

572 Our results demonstrate that *C. elegans* may use physical constraints on animal size and feeding rate to

573 control growth rate and determine developmental transitions. This type of regulation could be applicable to

574 organisms with stiff cuticles or other physical barriers to growth, like many species of Ecdysozoa. The control

575 of whole-organism growth requires cells, tissues, and organs to orchestrate final size and cell number. In *C.*

576 *elegans*, cell number is precisely defined and invariant from animal to animal (Horvitz and Sulston, 1980), so

577 the final adult size of an individual must come from cell size as opposed to number. Future studies should

578 focus on how whole-organism size is determined by the integration of cell, tissue, and organ size. By

579 incorporating these different developmental scales, the Stretcher model can be refined to completely describe

580 how physical constraints on parts of the organism impact the whole. *C. elegans* gives investigators a method to

581 investigate animal-to-animal variation in developmental trajectories across each of these scales.

582 # Methods

583 **Worm culture**

584 The canonical laboratory strain N2 was obtained from the *C. elegans* Natural Diversity Resource (Cook et al.,

585 2016). Animals were cultured at 20°C on 6 cm plates of modified nematode growth media (NGMA), which

586 contained 1% agar and 0.7% agarose seeded with *E. coli* OP50 bacteria (Andersen et al., 2014).

Bacterial food

E. coli HB101 bacteria were prepared from cultures grown for 15 hours in Superbroth and then pelleted by centrifugation. HB101 bacteria were diluted to OD100 in K medium (51 mM NaCl, 32 mM KCl, 3 mM CaCl2, and 3 mM MgSO4 in distilled water) and stored at -80°C. Bacteria were thawed and fed to animals at a concentration sufficient to sustain population growth from hatching to adulthood (OD20).

Growth of the animals

Populations of animals were propagated on NGMA plates for two generations without starvation. In the third generation, gravid adults were bleach-synchronized (Stiernagle, 2006). Embryos were resuspended in K medium, aliquoted into a 500 mL flask at a concentration of one embryo per µL, and allowed to hatch overnight. The following day, arrested L1s were fed HB101 bacteria at a final concentration of OD20 in a final flask volume of 100 mL K medium and HB101 food. Animals were grown for three days at 20°C with constant shaking. Following these three days, adult animals were bleach-synchronized once more and embryos were aliquoted to seven replicate 500 mL flasks at a concentration of one embryo per µL in 100 mL. The following morning, six flasks were fed HB101 bacterial food at a final concentration of OD20 in a final flask volume of 100 mL K medium and HB101 food. Two additional flasks were included to control for L1 animal size and possible clumping of bacterial food: one flask contained L1 larvae but did not have food added and one flask contained no larvae but the same concentration of HB101 bacteria as the six flasks containing L1 larvae. All replicate flasks were kept in an incubator at 20°C with shaking for the duration of the experiment. A small temperature gradient of 1.25°C was recorded in the shaking incubator with the highest temperature readings on the right side and lowest temperature readings on the left side (S1 File). This slight variation in temperature contributed to variation in developmental rate among replicates based on position within the incubator (replicates were placed in numerical order with replicate 1 positioned on the far right side of the incubator).

High-throughput measurements of body size and fluorescence

Flasks were sampled each hour beginning one hour after feeding and continuing for 72 consecutive hours. At each hour, 500 µL was removed from each flask and transferred to a well of a deep 96-well plate. Each flask was sampled at each time point. Fluorescent polychromatic beads (Polysciences, 19507-5) with a 0.5 µm particle size were added to each well at a final concentration of $3.64x10^8$ beads/mL and incubated at 20°C for 10 minutes with shaking. Following the bead incubation, 30 µL from each well of the deep 96-well plate was aliquoted to a 96-well microtiter plate. The process was repeated 11 times to 11 separate wells of the same microtiter plate with pipetting to mix the well contents from the deep 96-well plate. Animals were then treated with sodium azide at a final concentration of 50 mM to paralyze and prevent defecation of the ingested beads. The 96-well plate was imaged with an ImageXpress Nano (Molecular Devices, SanJose, CA) using both 2x (Nikon MRD00025) and 10x (Nikon MRH00101) objectives. The ImageXpress Nano acquires brightfield images using a 4.7 megaPixel CMOS camera. Images are stored in 16-bit TIFF format. Finally, animals were scored using a large-particle flow cytometer (COPAS BIOSORT, Union Biometrica, Holliston MA). The COPAS BIOSORT sheath flow rate was kept at a constant 10.3 ±0.1 mL per minute to reduce variability in length measurements.

Image processing

Manual measurements of animal size were performed using the free Java image-processing program ImageJ (Abràmoff et al., 2004). Well images for the six replicate flasks, excluding controls were loaded into ImageJ software. Length was measured from head to tail, and width was measured at the widest point of the animal. Five animals were measured per well across thirty total wells for each hour. Measurements were repeated for all 72 time points in the assay. Body length and width were used to estimate cross-sectional area (length*width). This metric was used to describe animal area for the extent of the text. Volume was calculated from body length and width by approximating the animal as a cylinder. Pixels were converted to µm using a conversion factor of 3.2937 pixels/µm.

34

Data processing

The COPAS BIOSORT was used to collect measurements of animal length (TOF), optical extinction (EXT), and fluorescence for every animal in each well. These traits measure properties of nematode development and, as such, increase as animals progress to adulthood (Andersen et al., 2015). Optical extinction measurements correspond to the amount of light absorbed over the full length of an animal as it passes through the instrument. An additional measurement (norm.EXT) can be calculated by normalizing optical extinction by length. The raw data collected were imported and processed using the *easysorter* R package (Shimko and Andersen, 2014).

The COPAS BIOSORT data were analyzed further using Gaussian finite mixture modeling as implemented in the *mclust* R package (Scrucca et al., 2016). These probabilistic models assume that data are generated from a mixture of multivariate normal distributions and, therefore, can be used to classify unstructured data into meaningful groups. Specifically, the *mclust* package fits a mixture model to data and selects the optimal number of clusters using an expectation-maximization algorithm and Bayes Information Criteria. For model-based clustering, log transformed animal length (logTOF) and log transformed optical extinction (logEXT) were used as inputs for the *Mclust* function. Data from each hour of the experiment was analyzed by replicate and clusters that did not appear to include majority animal objects were identified and removed as described previously (Smith et al., 2009). This processing removed non-animal objects such as bacterial clumps, shed cuticles, and next generation larval animals from the time-course data.

We used a numpy polyfit regression of well-median data from the COPAS BIOSORT and image measurements to convert TOF and norm.EXT data to microns (S5 File, Eq. S7-S9). Only the unit-corrected BIOSORT data were used for further analysis.

Molt analysis

Fluorescence data obtained from the COPAS BIOSORT was used as a proxy for feeding behavior to distinguish animals in a molt from growing animals. First, fluorescence was normalized by EXT to account for the ability of larger animals to consume more food and beads. Next, an analysis of variance statistical model was fit to the fluorescence data normalized by EXT to determine the amount of variance contributed by replicate and well (Table S1). A local kernel regression smoothing method was then applied to the residuals of the variance analysis using the *lokern* R package (Hermann, 2016). Residuals were used to address only the differences over time and ignore minor variation among replicates and wells. The local minima of the regression function were found by solving for where the first derivative of this function equaled zero. The time associated with each local minimum was used to represent the timing of each molt. Molts occurred at 14, 25, 36, and 48 hours.

To identify periods of time that contained a majority of growing animals, the inflection points of the regression function were calculated by solving for where the second derivative of the function equaled zero. Time points between inflection points that did not contain a local fluorescence minimum were considered as growth periods. These hours were 1-13, 17-22, 27-32, and 39-45 corresponding to L1, L2, L3, and L4 growth periods.

Each molt is initiated when animals enter lethargus: a behavioral state where animals cease active feeding. To classify individual animals as in a molt or growing, we set a quiescence threshold using fluorescence measurements at each local minimum. The fluorescence measurement at each local minimum was as follows: 0.07, 0.06, 0.06, 0.06. The average of these measurements (0.06) was used as the fluorescence threshold signifying quiescent behavior. Any individual animals that fell below this threshold fluorescence value were designated as in a molt and animals above this threshold value were classified as growing.

Comparison of model fits

To determine the volume growth model, we fit linear, exponential, and cubic functions to data designated as growth periods for each larval stage. Both linear and nonlinear functions were fitted using least-squares regression. Akaike's information criterion (AIC) (Sakamoto et al., 1986) and Bayesian information criterion (BIC) (Schwarz, 1978) were goodness of fit criteria used to evaluate candidate models. To assess the strength of evidence for each candidate model, we identified the model with the smallest AIC/BIC value and assessed the difference between this value and the AIC/BIC of the other two models. The magnitude of the difference was used to determine the level of support for each candidate model as previously described (Burnham and Anderson, 2007; Kass and Raftery, 1995). All model fits and analysis were performed using the *stats* R package.

Stretcher and feeding model analysis

To analyze shape dynamics, length and width data from growth time periods were extracted from the full COPAS BIOSORT population data and analyzed from each replicate separately to avoid issues with replicate variability. For replicate 2, the hours defining growth periods were 1-13, 16.37-22.39, and 26.93-32.96; corresponding to L1, L2, and L3. Hours defining larval stages were rounded as data was collected at exact hour increments. The L4 stage was excluded from the analysis because of the high variability within the population. We applied a local kernel regression, *lokern* R package ("Lokern: Kernel regression smoothing with local or global plug-in bandwidth," n.d.), to smooth the population dynamics of length and width. To calculate mean and standard deviation, the smoothed population measurements were bootstrapped using 2,000 samples with replacement (S5 File, Algorithm S1). To determine cuticle properties throughout larval stages, we calculated the mean ratio of derivatives of regression width and length. Error for this ratio was calculated using error propagation to pass the bootstrap variation through the ratio (S5 File, Eq. S24-28).

To analyze volumetric growth dynamics and feeding dynamics, volume regression was calculated using a cylindrical approximation for animal shape (S5 File, Eq. S7-S9) and the same local kernel regression

699 previously described was applied to red fluorescence data. Volume growth rate was calculated using the

700 python numpy gradient function applied to the volume regressions. An additional moving time window average

701 (1.4 hours) was applied to smooth numerical errors in the derivative when determining feeding and growth

702 regime transition points (S13 Fig).

References

Abràmoff MD, Magalhães PJ, Ram SJ. 2004. Image processing with ImageJ. *Biophotonics international* **11**:36–42.

Andersen EC, Bloom JS, Gerke JP, Kruglyak L. 2014. A variant in the neuropeptide receptor npr-1 is a major determinant of Caenorhabditis elegans growth and physiology. *PLoS Genet* **10**:e1004156.

Andersen EC, Shimko TC, Crissman JR, Ghosh R, Bloom JS, Seidel HS, Gerke JP, Kruglyak L. 2015. A Powerful New Quantitative Genetics Platform, Combining Caenorhabditis elegans High-Throughput Fitness Assays with a Large Collection of Recombinant Strains. *G3* **5**:911–920.

Avery L. 2003. Food transport in the C. elegans pharynx. *Journal of Experimental Biology*. doi:10.1242/jeb.00433

Baugh LR. 2013. To grow or not to grow: nutritional control of development during Caenorhabditis elegans L1 arrest. *Genetics* **194**:539–555.

Björklund M. 2019. Cell size homeostasis: Metabolic control of growth and cell division. *Biochim Biophys Acta Mol Cell Res* **1866**:409–417.

Brenner S. 1974. The genetics of Caenorhabditis elegans. *Genetics* **77**:71–94.

Broday L, Hauser CA, Kolotuev I, Ronai Z 'ev. 2007. Muscle-epidermis interactions affect exoskeleton patterning in Caenorhabditis elegans. *Dev Dyn* **236**:3129–3136.

Burnham KP, Anderson DR. 2007. Model Selection and Multimodel Inference: A Practical Information-Theoretic Approach. Springer Science & Business Media.

Byerly L, Cassada RC, Russell RL. 1976. The life cycle of the nematode Caenorhabditis elegans. I. Wild-type growth and reproduction. *Dev Biol* **51**:23–33.

Cadart C, Monnier S, Grilli J, Sáez PJ, Srivastava N, Attia R, Terriac E, Baum B, Cosentino-Lagomarsino M, Piel M. 2018. Size control in mammalian cells involves modulation of both growth rate and cell cycle duration. *Nat Commun* **9**:3275.

Campos M, Surovtsev IV, Kato S, Paintdakhi A, Beltran B, Ebmeier SE, Jacobs-Wagner C. 2014. A constant size extension drives bacterial cell size homeostasis. *Cell* **159**:1433–1446.

Cassada RC, Russell RL. 1975. The dauerlarva, a post-embryonic developmental variant of the nematode Caenorhabditis elegans. *Dev Biol* **46**:326–342.

Cook DE, Zdraljevic S, Tanny RE, Seo B, Riccardi DD, Noble LM, Rockman MV, Alkema MJ, Braendle C, Kammenga JE, Wang J, Kruglyak L, Félix M-A, Lee J, Andersen EC. 2016. The Genetic Basis of Natural Variation in Caenorhabditis elegans Telomere Length. *Genetics* **204**:371–383.

Costa M, Draper BW, Priess JR. 1997. The role of actin filaments in patterning the Caenorhabditis elegans cuticle. *Dev Biol* **184**:373–384.

Cox GN, Staprans S, Edgar RS. 1981. The cuticle of Caenorhabditis elegans. II. Stage-specific changes in ultrastructure and protein composition during postembryonic development. *Dev Biol* **86**:456–470.

Dodd W, Tang L, Lone J-C, Wimberly K, Wu C-W, Consalvo C, Wright JE, Pujol N, Choe KP. 2018. A Damage Sensor Associated with the Cuticle Coordinates Three Core Environmental Stress Responses in Caenorhabditis elegans. *Genetics* **208**:1467–1482.

Donnan L, John PC. 1983. Cell cycle control by timer and sizer in Chlamydomonas. *Nature* **304**:630–633.

Essmann CL, Elmi M, Shaw M, Anand GM, Pawar VM, Srinivasan MA. 2017. In-vivo high resolution AFM topographic imaging of Caenorhabditis elegans reveals previously unreported surface structures of cuticle mutants. *Nanomedicine* **13**:183–189.

Fang-Yen C, Avery L, Samuel ADT. 2009. Two size-selective mechanisms specifically trap bacteria-sized food particles in Caenorhabditis elegans. *Proc Natl Acad Sci U S A* **106**:20093–20096.

Gilpin W, Uppaluri S, Brangwynne CP. 2015. Worms under Pressure: Bulk Mechanical Properties of C. elegans Are Independent of the Cuticle. *Biophysical Journal*. doi:10.1016/j.bpj.2015.03.020

Golden JW, Riddle DL. 1984. The Caenorhabditis elegans dauer larva: developmental effects of pheromone, food, and temperature. *Dev Biol* **102**:368–378.

Hermann E. 2016. lokern: Kernel Regression Smoothing with Local or Global Plug-in Bandwidth. R package

752   version 1.1-8. https://CRAN.R-project.org/package=lokern

753 Holzapfel GA. 2017. Similarities between soft biological tissues and rubberlike materials. *Constitutive Models*
754   *for Rubber IV* 607–617.

755 Hone DWE, Benton MJ. 2005. The evolution of large size: how does Cope's Rule work? *Trends Ecol Evol*
756   **20**:4–6.

757 Horvitz HR, Sulston JE. 1980. Isolation and genetic characterization of cell-lineage mutants of the nematode
758   Caenorhabditis elegans. *Genetics* **96**:435–454.

759 Hu PJ. 2018. Dauer. WormBook.

760 Jorgensen P, Tyers M. 2004. How cells coordinate growth and division. *Curr Biol* **14**:R1014–27.

761 Kass RE, Raftery AE. 1995. Bayes Factors. *J Am Stat Assoc* **90**:773.

762 Katz SS, Maybrun C, Maul-Newby HM, Frand AR. 2018. Non-canonical apical constriction shapes emergent
763   matrices in C. elegans. *bioRxiv*. doi:10.1101/189951

764 Knight CG, Patel MN, Azevedo RBR, Leroi AM. 2002. A novel mode of ecdysozoan growth in Caenorhabditis
765   elegans. *Evol Dev* **4**:16–27.

766 Lokern: Kernel regression smoothing with local or global plug-in bandwidth. n.d.
767   https://CRAN.R-project.org/package=lokern

768 Madaan U, Faure L, Chowdhury A, Ahmed S, Ciccarelli EJ, Gumienny TL, Savage-Dunn C. 2020. Feedback
769   regulation of BMP signaling by cuticle collagens. *Mol Biol Cell* **31**:825–832.

770 Madaan U, Yzeiraj E, Meade M, Clark JF, Rushlow CA, Savage-Dunn C. 2018. BMP Signaling Determines
771   Body Size via Transcriptional Regulation of Collagen Genes in Caenorhabditis elegans. *Genetics*
772   **210**:1355–1367.

773 McKeown C, Praitis V, Austin J. 1998. sma-1 encodes a betaH-spectrin homolog required for Caenorhabditis
774   elegans morphogenesis. *Development* **125**:2087–2098.

775 Moerman DG, Williams BD. 2006. Sarcomere assembly in C. elegans muscle. *WormBook* 1–16.

776 Monsalve GC, Van Buskirk C, Frand AR. 2011. LIN-42/PERIOD controls cyclical and developmental
777   progression of C. elegans molts. *Curr Biol* **21**:2033–2045.

778 Mörck C, Pilon M. 2006. C. elegans feeding defective mutants have shorter body lengths and increased
779   autophagy. *BMC Dev Biol* **6**:39.

780 Moss-Taylor L, Upadhyay A, Pan X, Kim M-J, O'Connor MB. 2019. Body Size and Tissue-Scaling Is Regulated
781   by Motoneuron-Derived Activinß in Drosophila melanogaster. *Genetics* **213**:1447–1464.

782 Nika L, Gibson T, Konkus R, Karp X. 2016. Fluorescent Beads Are a Versatile Tool for Staging Caenorhabditis
783   elegans in Different Life Histories. *G3* **6**:1923–1933.

784 Osella M, Nugent E, Cosentino Lagomarsino M. 2014. Concerted control of Escherichia coli cell division. *Proc*
785   *Natl Acad Sci U S A* **111**:3431–3435.

786 Page AP, Johnstone IL. 2007a. The cuticle. *WormBook* 1–15.

787 Page AP, Johnstone IL. 2007b. The cuticle. WormBook.

788 Park S-J, Goodman MB, Pruitt BL. 2007. Analysis of nematode mechanics by piezoresistive displacement
789   clamp. *Proc Natl Acad Sci U S A* **104**:17376–17381.

790 Patterson GI, Padgett RW. 2000. TGF beta-related pathways. Roles in Caenorhabditis elegans development.
791   *Trends Genet* **16**:27–33.

792 Pavelescu I, Vilarrasa-Blasi J, Planas-Riverola A, González-García M-P, Caño-Delgado AI, Ibañes M. 2018. A
793   Sizer model for cell differentiation in Arabidopsis thaliana root growth. *Mol Syst Biol* **14**:e7687.

794 Petzold BC, Park S-J, Ponce P, Roozeboom C, Powell C, Goodman MB, Pruitt BL. 2011. Caenorhabditis
795   elegans body mechanics are regulated by body wall muscle tone. *Biophys J* **100**:1977–1985.

796 Pulak R. 2006. Techniques for Analysis, Sorting, and Dispensing of C. elegans on the COPAS™ Flow-Sorting
797   System In: Strange K, editor. C. Elegans: Methods and Applications. Totowa, NJ: Humana Press. pp.
798   275–286.

799 Sakamoto Y, Ishiguro M, Kitagawa G. 1986. Akaike information criterion statistics. *Dordrecht, The Netherlands:*
800   *D Reidel* **81**:26853.

801 Schiller HB, Fässler R. 2013. Mechanosensitivity and compositional dynamics of cell-matrix adhesions. *EMBO*
802   *Rep* **14**:509–519.

803 Schwarz G. 1978. Estimating the Dimension of a Model. *aos* **6**:461–464.

804 Scrucca L, Fop M, Murphy TB, Raftery AE. 2016. mclust 5: Clustering, Classification and Density Estimation
805   Using Gaussian Finite Mixture Models. *R J* **8**:289–317.
806 Shimko TC, Andersen EC. 2014. COPASutils: An R Package for Reading, Processing, and Visualizing Data
807   from COPAS Large-Particle Flow Cytometers. *PLoS ONE*. doi:10.1371/journal.pone.0111090
808 Singh RN, Sulston JE. 1978. Some Observations On Moulting in Caenorhabditis Elegans. *Nematologica*
809   **24**:63–71.
810 Smith MV, Boyd WA, Kissling GE, Rice JR, Snyder DW, Portier CJ, Freedman JH. 2009. A discrete time model
811   for the analysis of medium-throughput C. elegans growth data. *PLoS One* **4**:e7018.
812 Soifer I, Robert L, Amir A. 2016. Single-Cell Analysis of Growth in Budding Yeast and Bacteria Reveals a
813   Common Size Regulation Strategy. *Curr Biol* **26**:356–361.
814 Spence AJ. 2009. Scaling in biology. *Curr Biol* **19**:R57–61.
815 Stiernagle T. 2006. Maintenance of C. elegans. WormBook.
816 Sulston JE, Horvitz HR. 1977. Post-embryonic cell lineages of the nematode, Caenorhabditis elegans. *Dev Biol*
817   **56**:110–156.
818 Suman SK, Daday C, Ferraro T, Vuong-Brender T, Tak S, Quintin S, Robin F, Gräter F, Labouesse M. 2019.
819   The plakin domain of VAB-10/plectin acts as a hub in a mechanotransduction pathway to promote
820   morphogenesis. *Development* **146**. doi:10.1242/dev.183780
821 Sveiczer A, Novak B, Mitchison JM. 1996. The size control of fission yeast revisited. *J Cell Sci* **109 (Pt**
822   **12)**:2947–2957.
823 Taheri-Araghi S, Bradde S, Sauls JT, Hill NS, Levin PA, Paulsson J, Vergassola M, Jun S. 2015. Cell-size
824   control and homeostasis in bacteria. *Curr Biol* **25**:385–391.
825 Towbin BD, Grosshans H. 2021. A folder mechanism ensures size uniformity among C. elegans individuals by
826   coupling growth and development. *bioRxiv*.
827 Tuck S. 2014. The control of cell growth and body size in Caenorhabditis elegans. *Exp Cell Res* **321**:71–76.
828 Turner JJ, Ewald JC, Skotheim JM. 2012. Cell size control in yeast. *Curr Biol* **22**:R350–9.
829 Tzur A, Kafri R, LeBleu VS, Lahav G, Kirschner MW. 2009. Cell growth and size homeostasis in proliferating
830   animal cells. *Science* **325**:167–171.
831 Uppaluri S, Brangwynne CP. 2015. A size threshold governs Caenorhabditis elegans developmental
832   progression. *Proc Biol Sci* **282**:20151283.
833 Uppaluri S, Weber SC, Brangwynne CP. 2016. Hierarchical Size Scaling during Multicellular Growth and
834   Development. *Cell Rep* **17**:345–352.
835 Vuaridel-Thurre G, Vuaridel AR, Dhar N, McKinney JD. 2020. Computational Analysis of the Mutual
836   Constraints between Single-Cell Growth and Division Control Models. *Adv Biosyst* **4**:e1900103.
837 Wang P, Hayden S, Masui Y. 2000. Transition of the blastomere cell cycle from cell size-independent to
838   size-dependent control at the midblastula stage in Xenopus laevis. *J Exp Zool* **287**:128–144.
839 Wang P, Robert L, Pelletier J, Dang WL, Taddei F, Wright A, Jun S. 2010. Robust growth of Escherichia coli.
840   *Curr Biol* **20**:1099–1103.
841 Willis L, Huang KC. 2017. Sizing up the bacterial cell cycle. *Nat Rev Microbiol* **15**:606–620.
842 Wolfenson H, Bershadsky A, Henis YI, Geiger B. 2011. Actomyosin-generated tension controls the molecular
843   kinetics of focal adhesions. *J Cell Sci* **124**:1425–1432.
844 Wood WB. 1988. The Nematode Caenorhabditis Elegans. Cold Spring Harbor Laboratory.
845 Yochem J, Lažetić V, Bell L, Chen L, Fay D. 2015. C. elegans NIMA-related kinases NEKL-2 and NEKL-3 are
846   required for the completion of molting. *Dev Biol* **398**:255–266.
847 Zaidel-Bar R, Miller S, Kaminsky R, Broday L. 2010. Molting-specific downregulation of C. elegans body-wall
848   muscle attachment sites: the role of RNF-5 E3 ligase. *Biochem Biophys Res Commun* **395**:509–514.
849 Zhang H, Landmann F, Zahreddine H, Rodriguez D, Koch M, Labouesse M. 2011. A tension-induced
850   mechanotransduction pathway promotes epithelial morphogenesis. *Nature* **471**:99–103.

Data availability

The authors state that all data necessary to confirm the conclusions of this work are within the text, figures, and supporting information files. All files and code for analysis and generation of figures and tables are archived on GitHub (https://github.com/AndersenLab/C.elegans-growth-manuscript).

Acknowledgements

Competing interests: The authors have no competing interests.

870 **Supporting Information Captions**
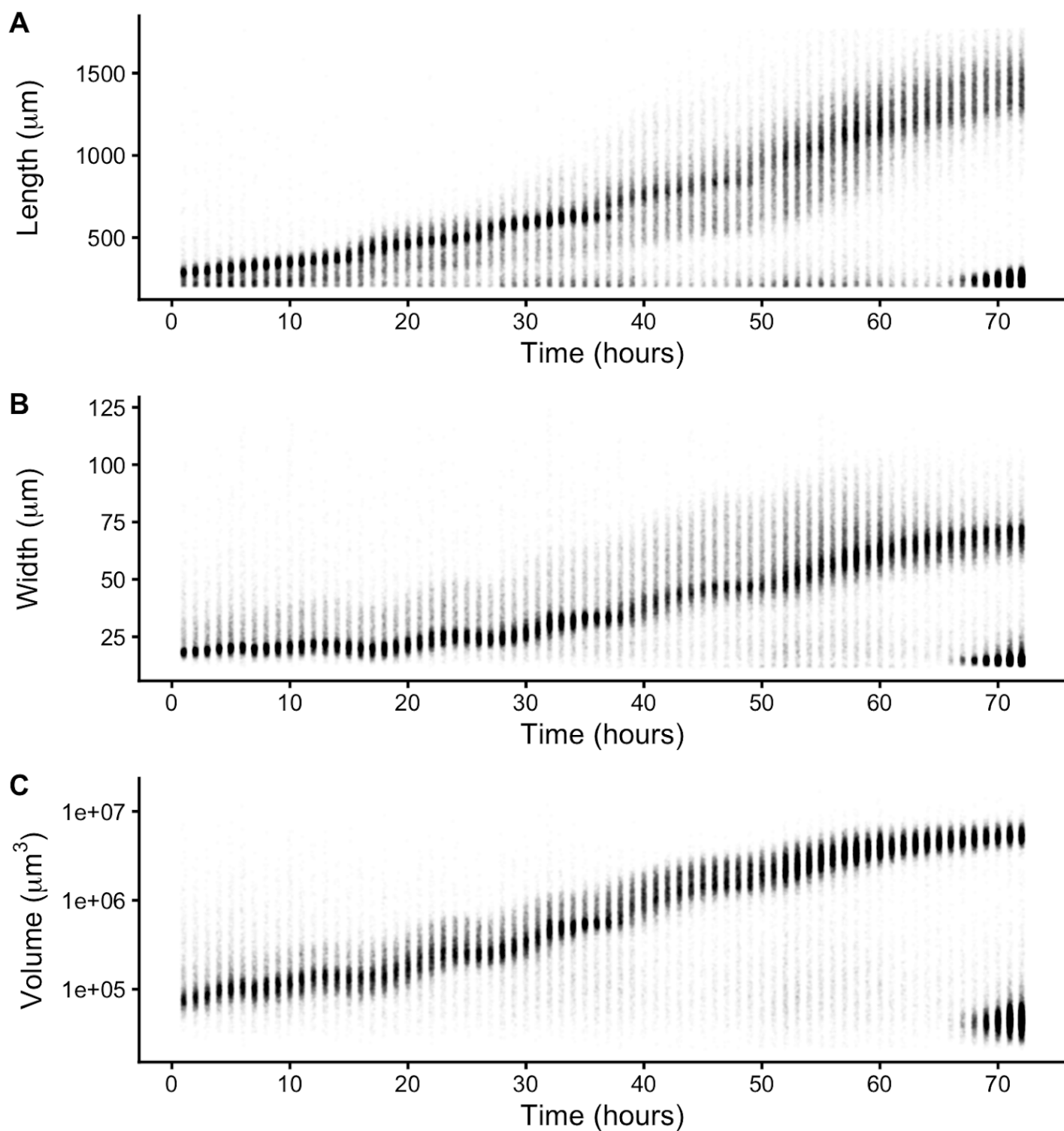
872 **S1 Fig. Raw measurements of animal size.** Raw COPAS BIOSORT data of animal length (A), width (B), and
873 volume (C) are shown here. After 60 hours, animals have developed to the adult stage. Smaller objects
874 observed after 65 hours were the next generation of newly hatched L1 larvae laid by the animals that
875 developed during the time course.
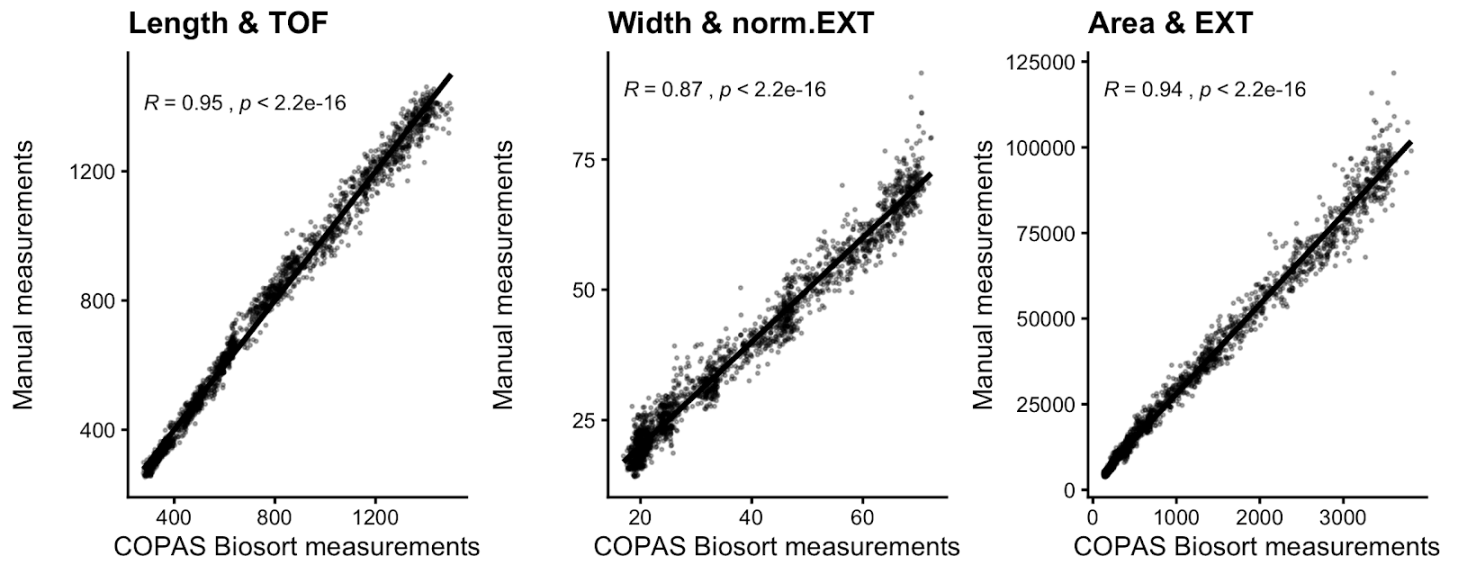
S2 Fig. Correlation analysis of body size measurements. Manual measurements of animal length, width, and estimated area were compared to COPAS BIOSORT measurements of TOF, norm.EXT, and EXT. Kendall correlation value is shown in each plot.
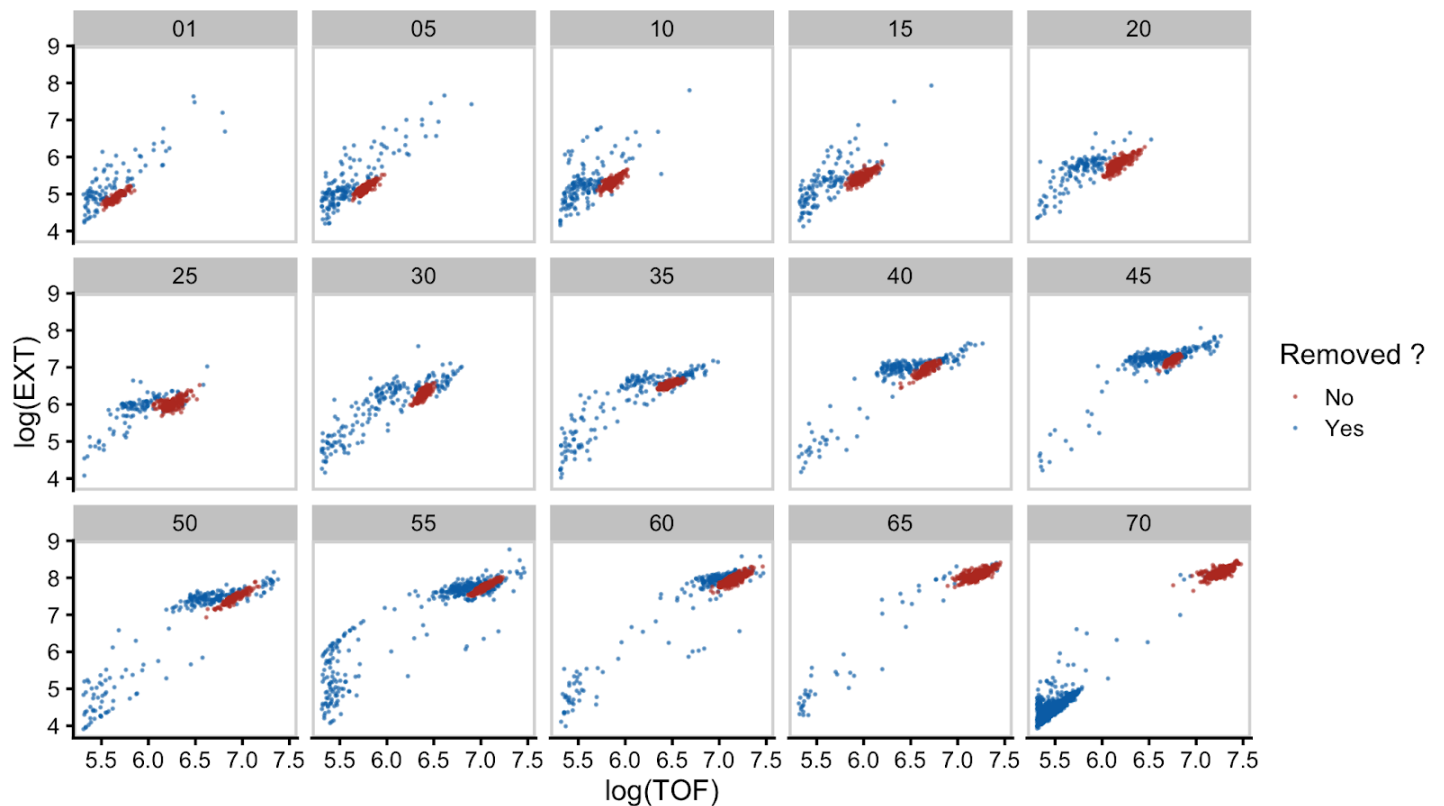
S3 Fig. Mixture modeling of COPAS BIOSORT data was used to prune data. Mixture models of Gaussian distributions were fit to log transformed animal length (x-axis) and log transformed optical extinction (y-axis). Data from each hour of the experiment was analyzed and processed to remove clusters that did not include animal objects. All replicates were pruned independently; a subset of data from replicate 2 is shown here. Panels indicate experimental hours from which data were taken.

44
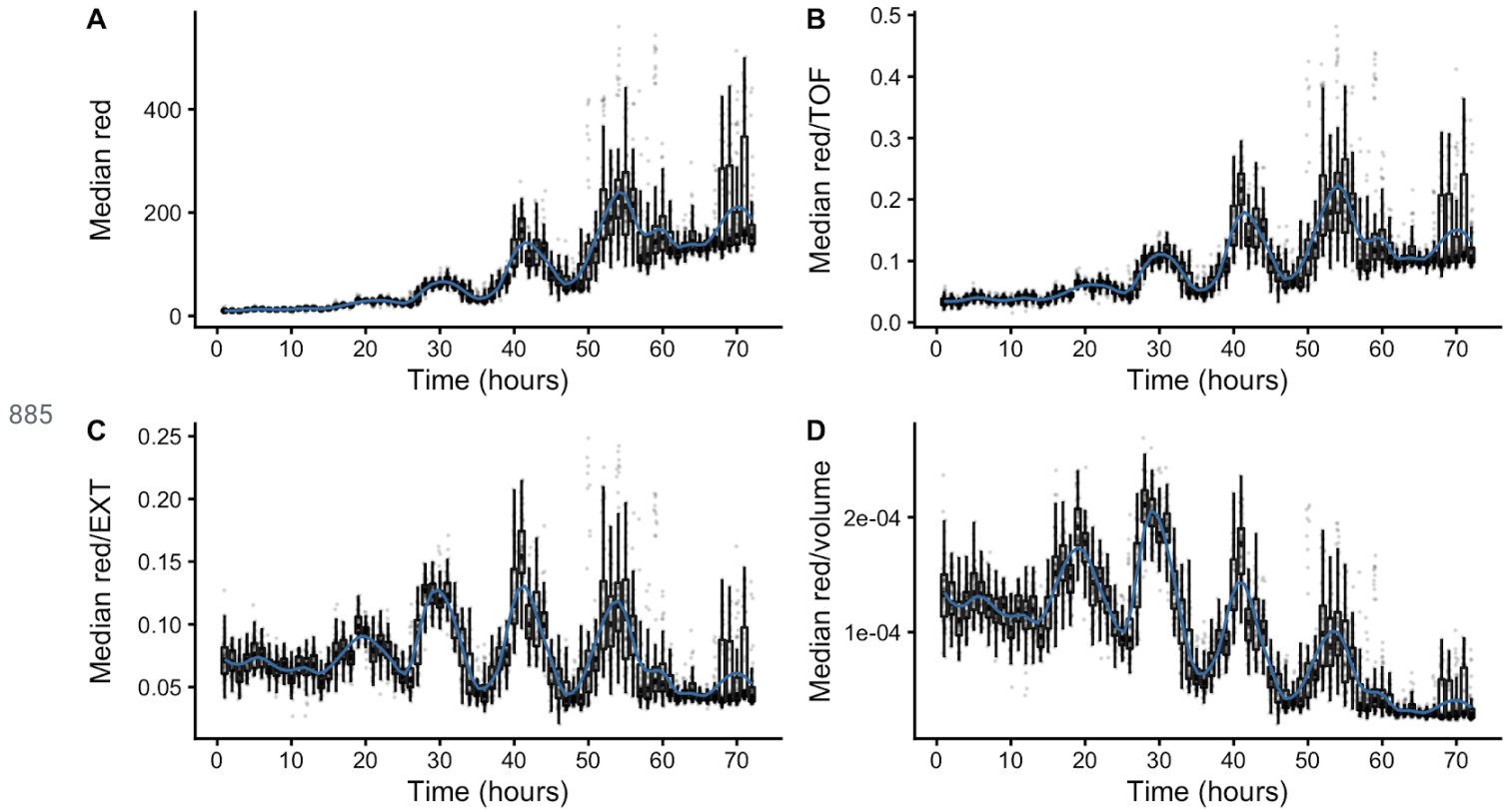
S4 Fig. Fluorescence measurements normalized by body size. Red fluorescence beads were fed to animals during experimentation and fluorescence data was collected by the COPAS BIOSORT. Fluctuations in fluorescence indicate fluctuations in feeding behavior. Fluorescence data was normalized by body size measurements to account for increases in body size. Dividing fluorescence by area was most successful in normalizing fluorescence dynamics to account for changes in animal size over time.
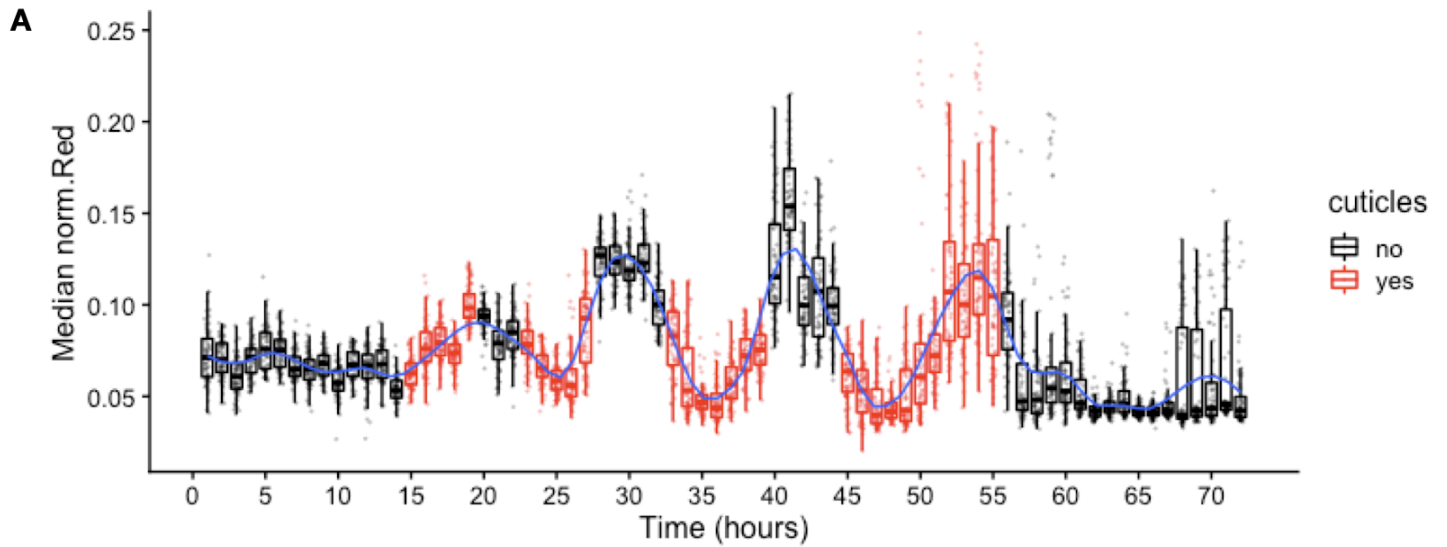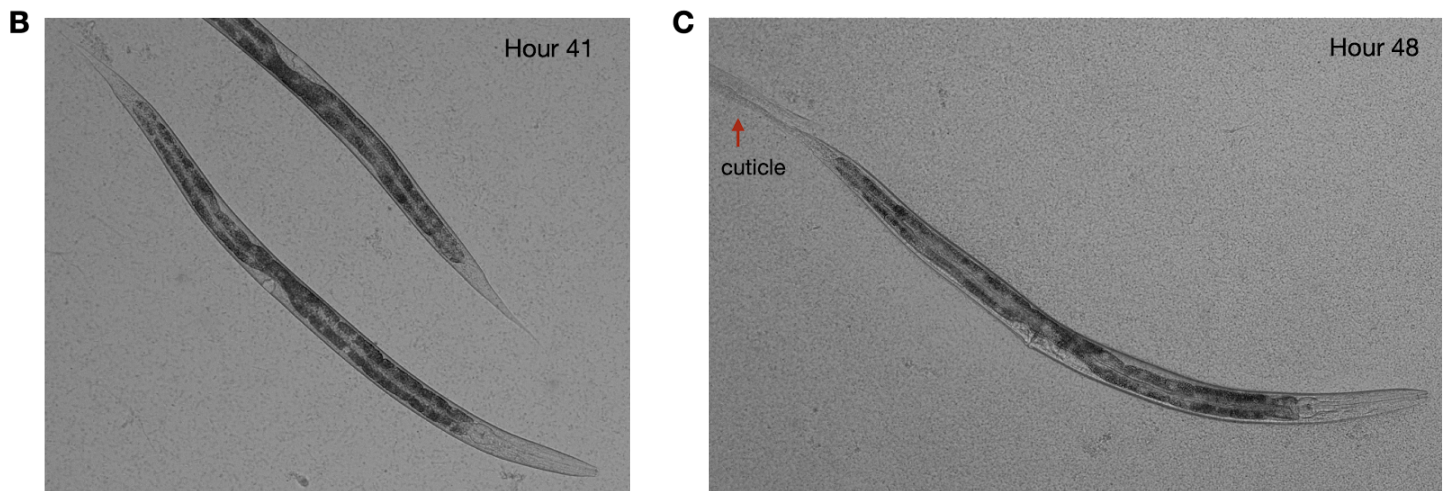
S5 Fig. Cuticles identified during periods of decreased feeding. Images of wells collected during the experiment were examined for evidence of shed cuticles. (A) Experimental hours where cuticles were identified from images overlap with hours where population feeding behavior is low. Cuticles shed from the L4-Adult molt persisted longer than previous larval stage cuticle debri. (B) Example image of animal without visible cuticle during a period of elevated feeding. (C) Example image of an animal with visible cuticle indicating completion of molt during a period of decreased feeding.

46
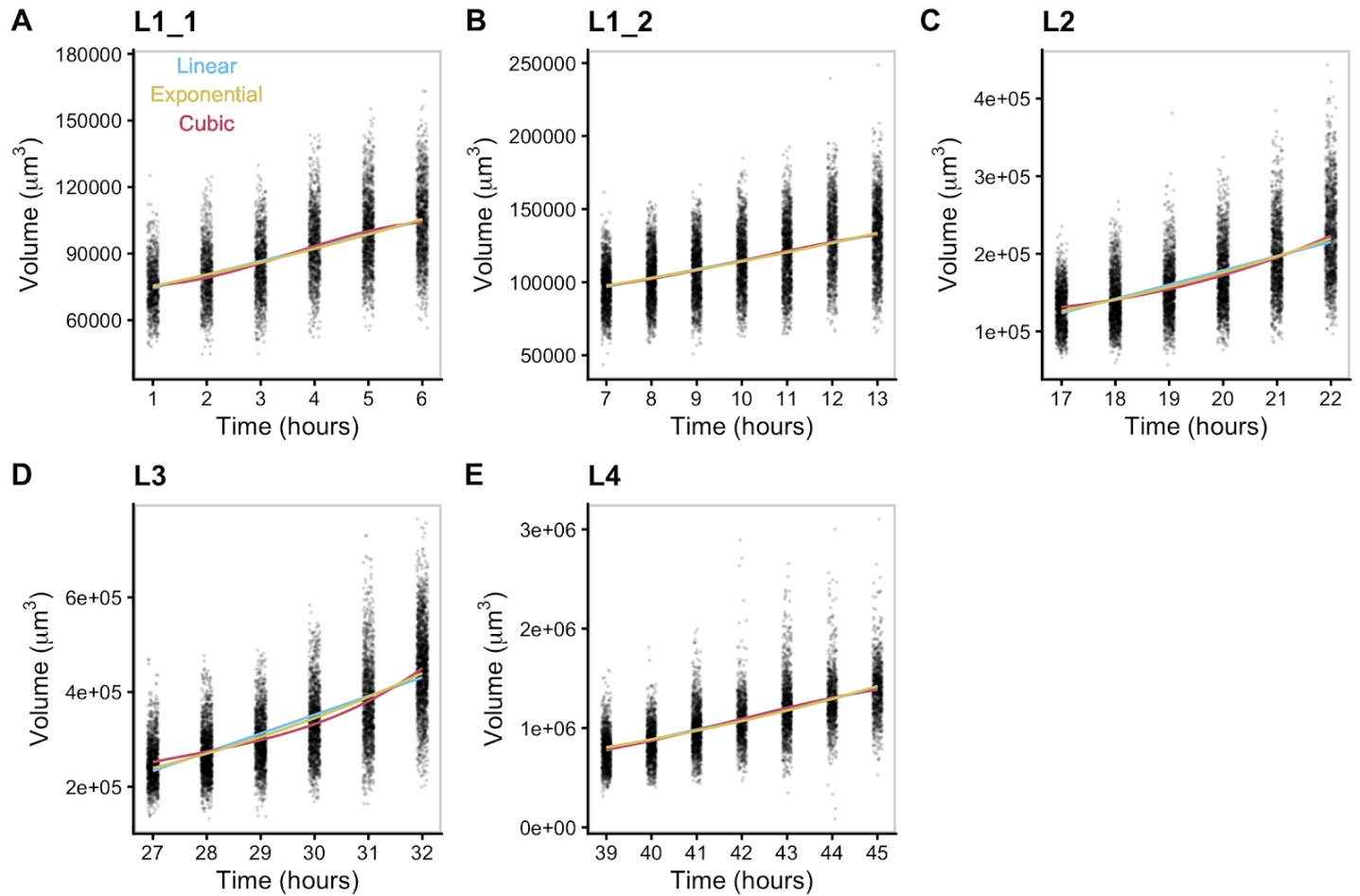
S6 Fig. Volume growth data fit with linear, exponential, and cubic models. Volume data of individuals in time points defined as growth periods are analyzed for each stage. L1 stage was further separated into two periods to account for the volume dip that occurs mid-stage.

47
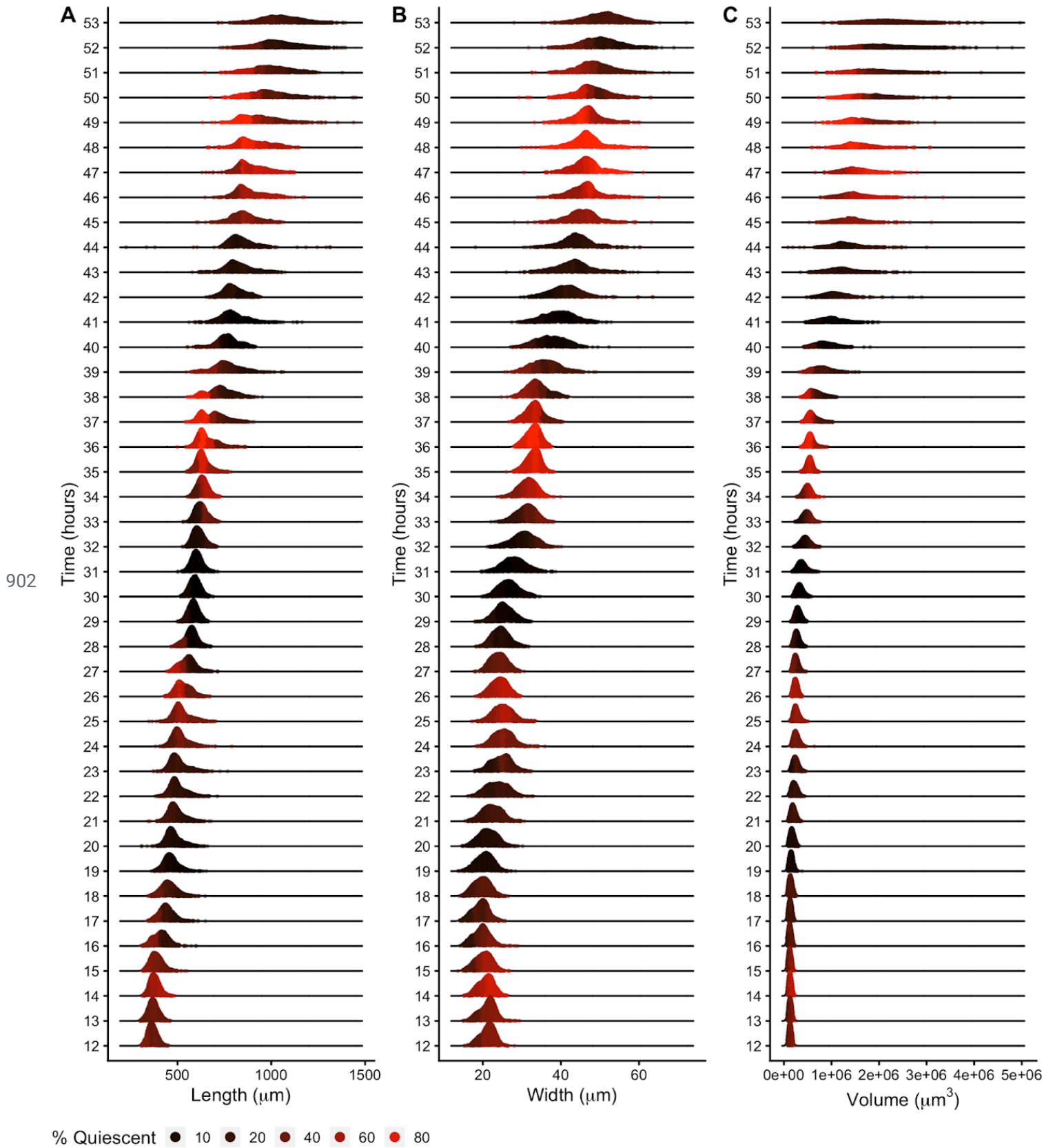
S7 Fig. Density plots of population size dynamics across all larval transitions. Density curves of length (A), width (B) and volume (C). Curves are divided into five quantiles and colored by the percentage of quiescent animals present within that quantile. Molts are estimated to occur at experimental hours 14, 25, 36, and 48 (see Methods).

48
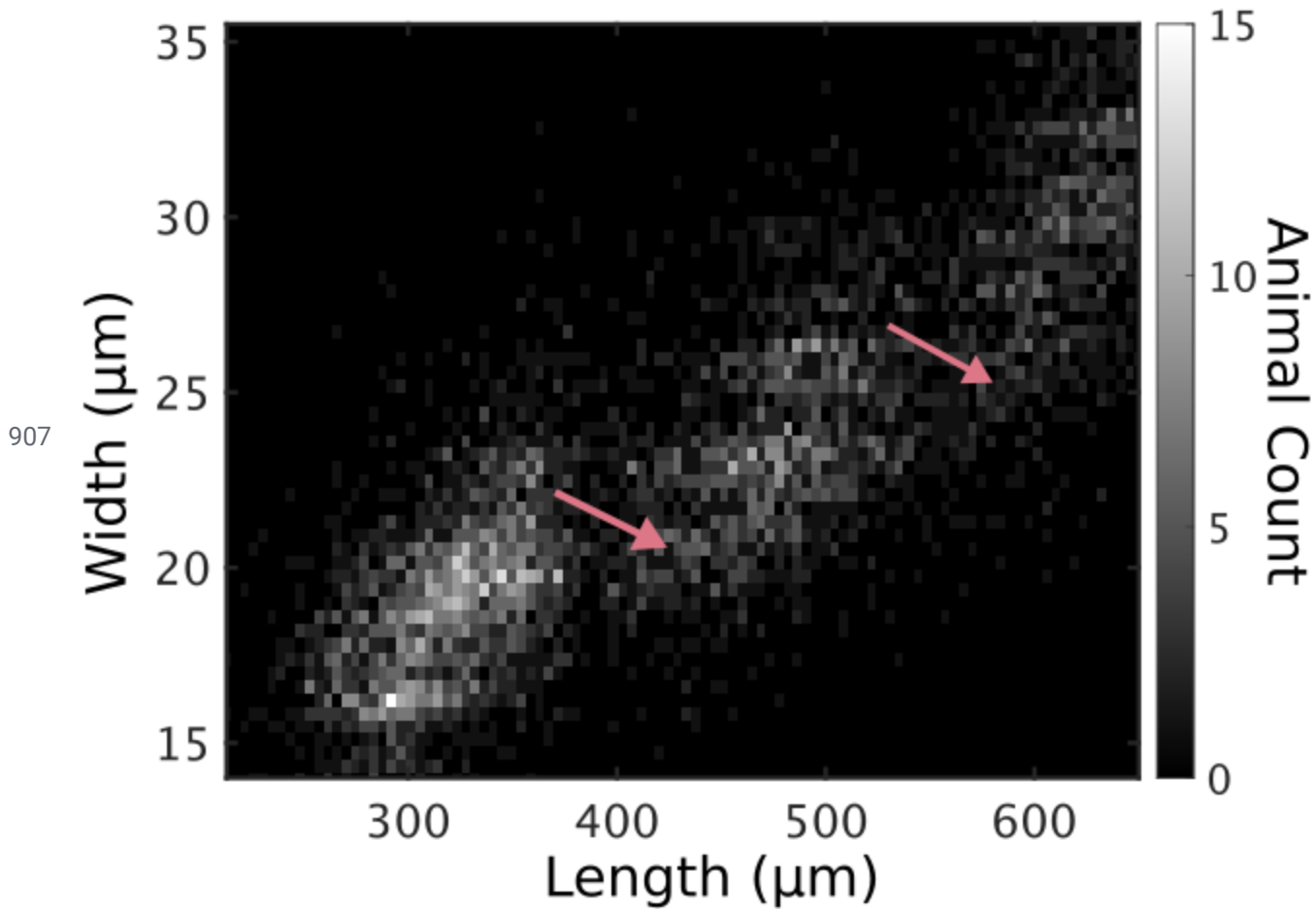
S8 Fig.

Animals in all replicates, measured from images. Animal length and width over *C. elegans* development captured from image data. Higher noise levels in these measurements preclude accurate regressions to individual larval stages. Length jumps and width dips are still apparent. Compare with Fig 6**.**
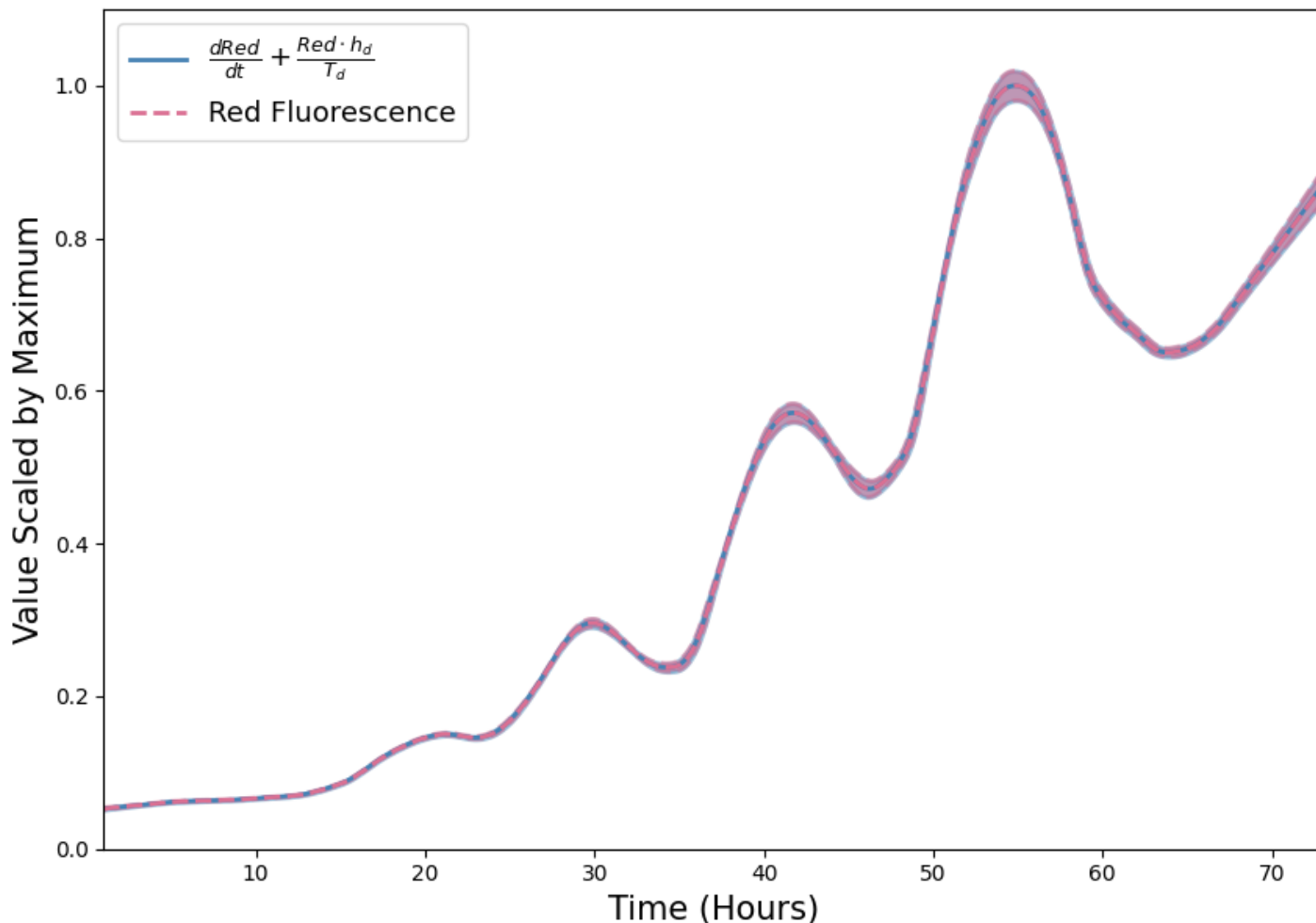
S9 Fig. Comparison of red fluorescence regression and food intake rate with defecation calculation. Regression of red fluorescence (dashed pink) is compared to the intake rate of red beads accounting for defecation rate (blue). Overlap of these two curves validates the use of red fluorescence as a proxy for food
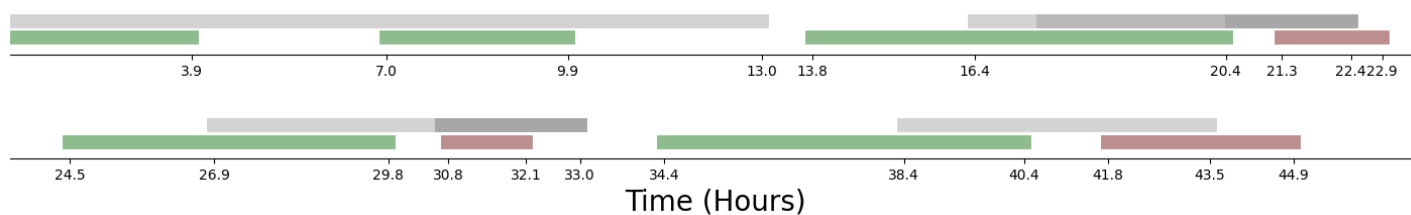
S10 Fig. Timeline of Food Utilization and Stretcher events. In the first row (grey and white), we mark the slopes determined in the Stretcher model. Transition from lighter to darker grey indicates a step increase in slope corresponding to a stiffening cuticle in the length direction. White regions denote time between larval stages. L2 and L3 are the only stages at which we have useful slope information due to the change in slope observed during L1 making transitions difficult to determine and the high level of population desynchronization in L4. In the second row (green, red, and white), we mark the food and growth correlations found in Fig 5B. Green corresponds to times at which both growth rate and food rate are increasing. Red corresponds to times at which both growth rate and food rate are decreasing. White corresponds to times at which growth rate and food rate are uncorrelated. Transitions from green to red regions occur at roughly the same times as the transition to a stiffer cuticle in the length direction.

50
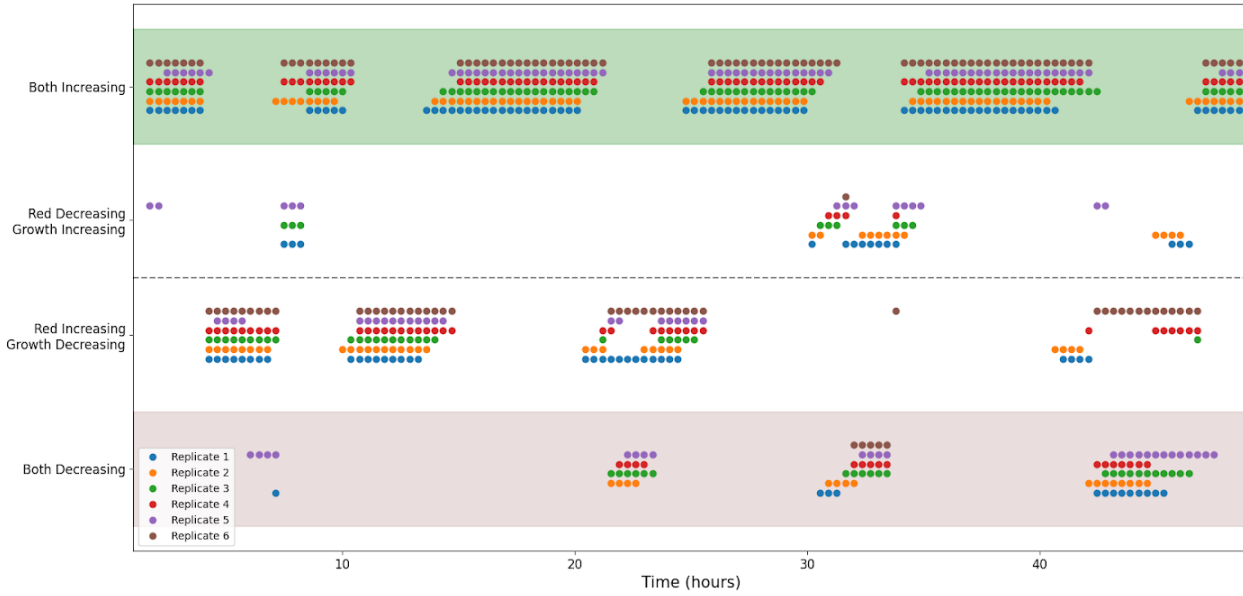
S11 Fig. Analysis of Food intake and growth rate correlation for all replicates. Summary of analysis in Fig. 8 for all replicates. Until larval stage L4, most replicates followed the same pattern of transitions from one growth regime to the next. The time delay at transitions in later replicates can be explained by the temperature gradient and differences in growth between replicates.

931
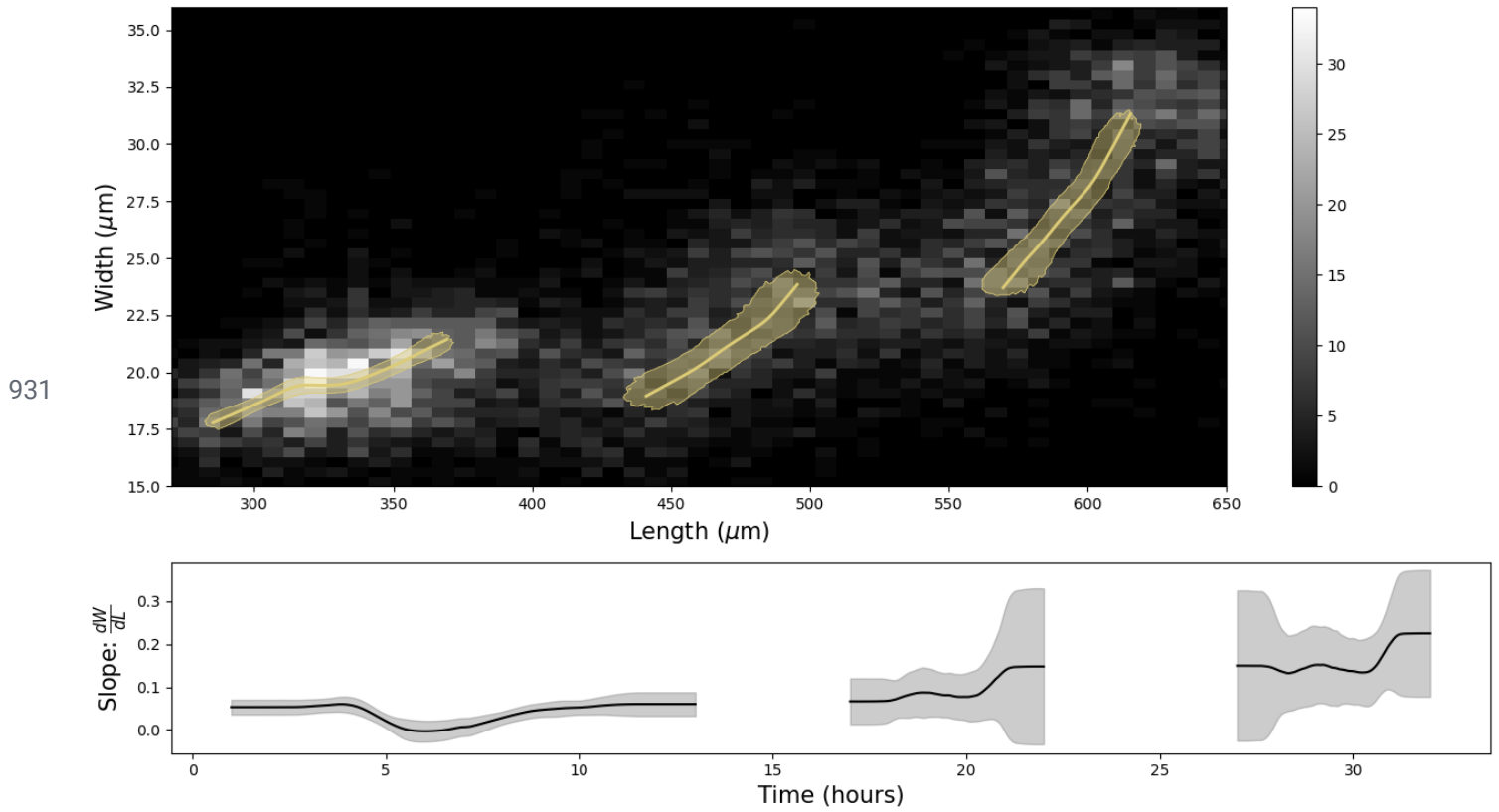
S12 Fig. Stretcher model analysis of replicate 2 COPAS BIOSORT data for different stage thresholding. Compare to Fig 5**.** Larval hours were defined by taking the ceiling of the lower boundary and the floor of the upper boundary. This rounding method for larval stage definition demonstrates the sensitivity of the analysis to edge effects. The unexpected step in the L2 larval stage (Fig 5) was significantly reduced with this rounding method.
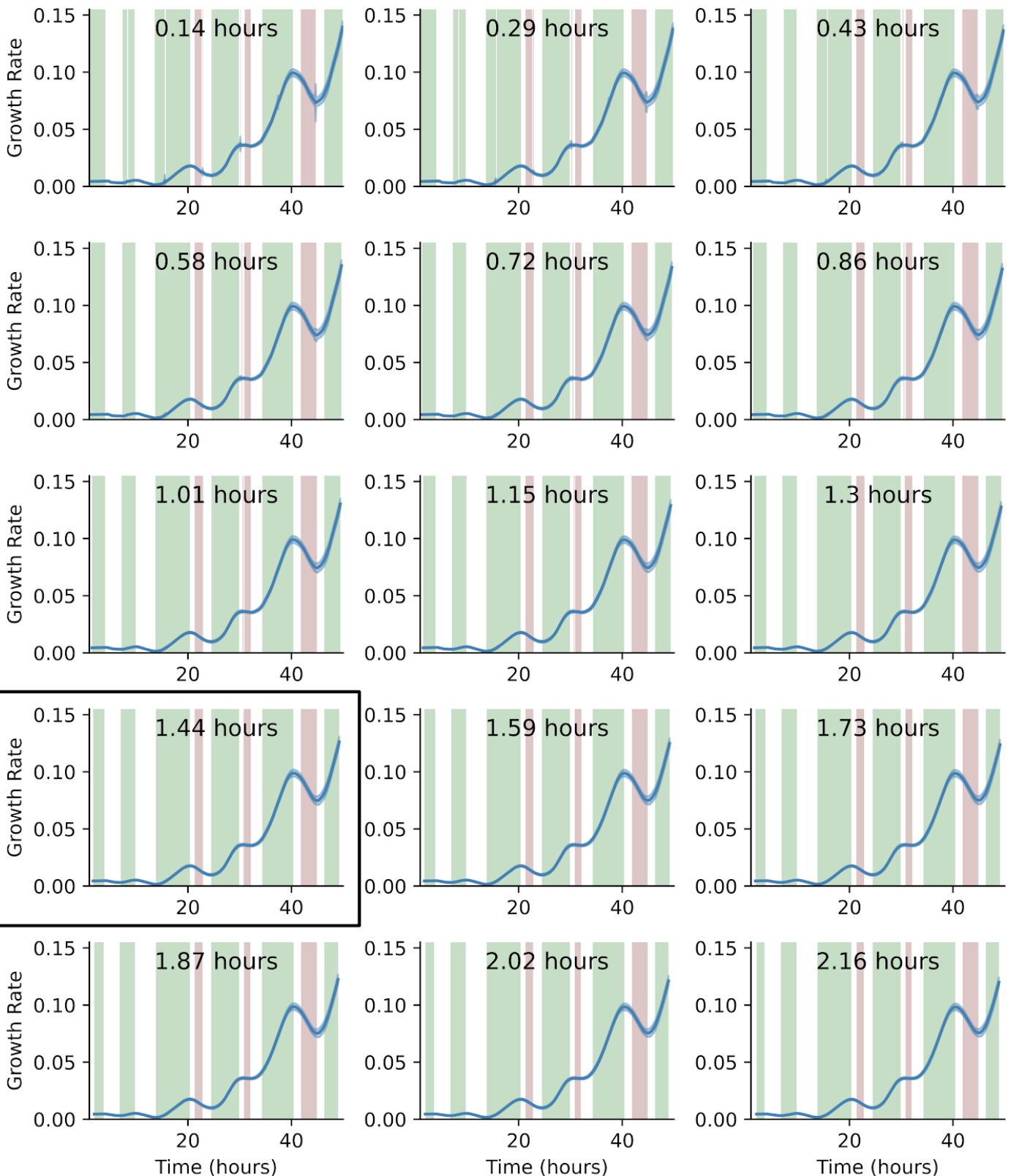
S13 Fig. Sensitivity analysis to moving average window size. Varying lengths of window sizes (0.14 to 2.16 hours) were calculated for the *lokern* growth rate regression. Window size was increased until the growth rate regression was smoothed. A window size of 1.44 hours (or 0.72 hours on either side of each time point) was chosen to calculate the start and end times of each regime (Fig 8). Continued increase of window size past 1.44 hours did not change the pattern of regimes or their boundaries significantly.
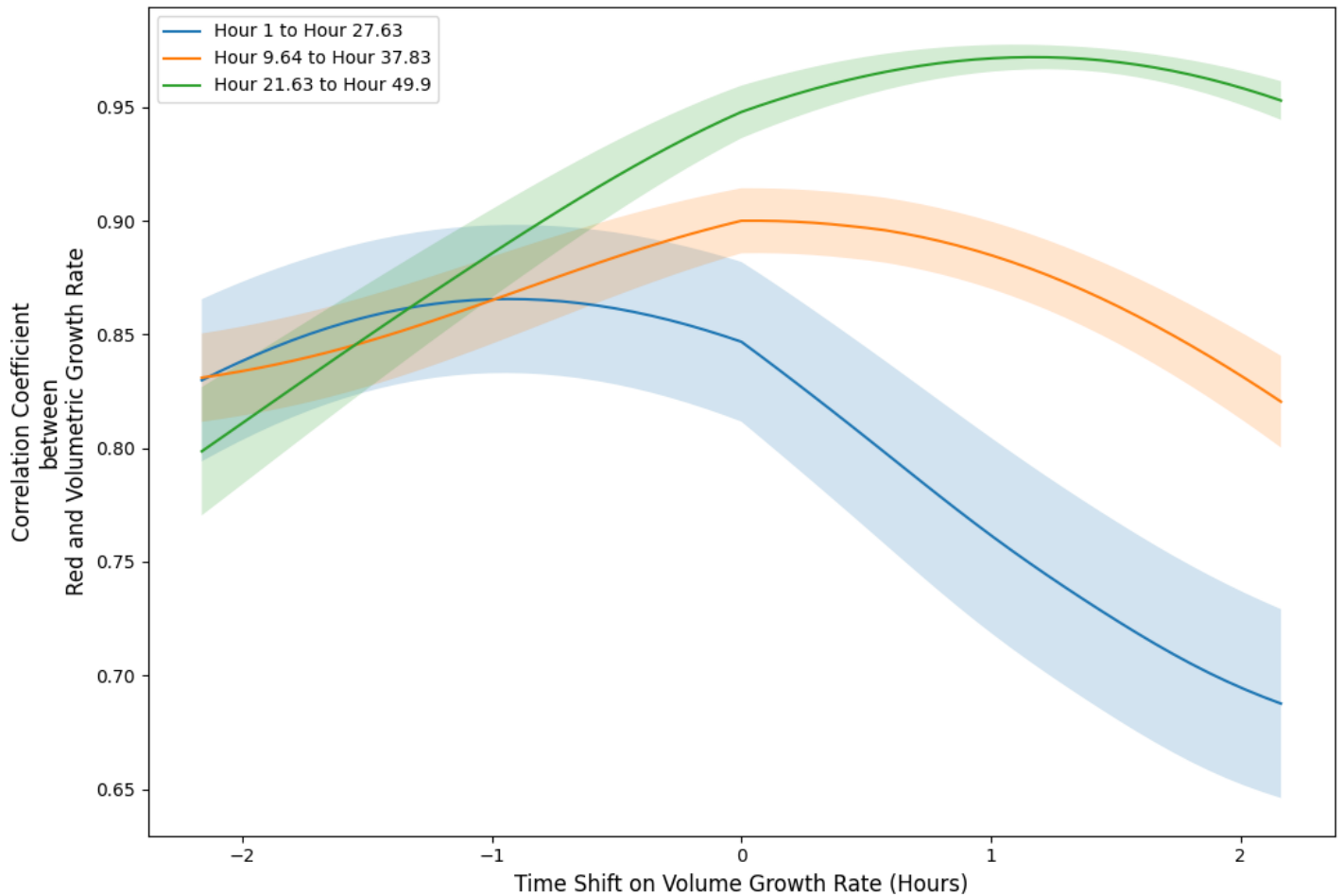
S14 Fig. Time Lag Analysis. Subsections of food intake rate and growth rate regressions were compared to determine the existing time lag between the two curves. The time shift is applied to the volume growth rate. A correlation coefficient was calculated for the new volume growth rate curve and the untouched red fluorescence regression curve for each bootstrap regression. The solid line corresponds to the mean of all the correlation coefficients over the bootstrapping iterations and the shaded regions correspond to the standard deviation. The blue curve corresponds to hours containing L1 and L2, the orange curve corresponds to hours containing L2 and L3, and the green curve corresponds to hours containing L3 and L4. The time lag at which the correlation between Red fluorescence and volume growth rate is at a maximum corresponds to the apparent time lag between the two curves. No single time lag captures the entirety of development.
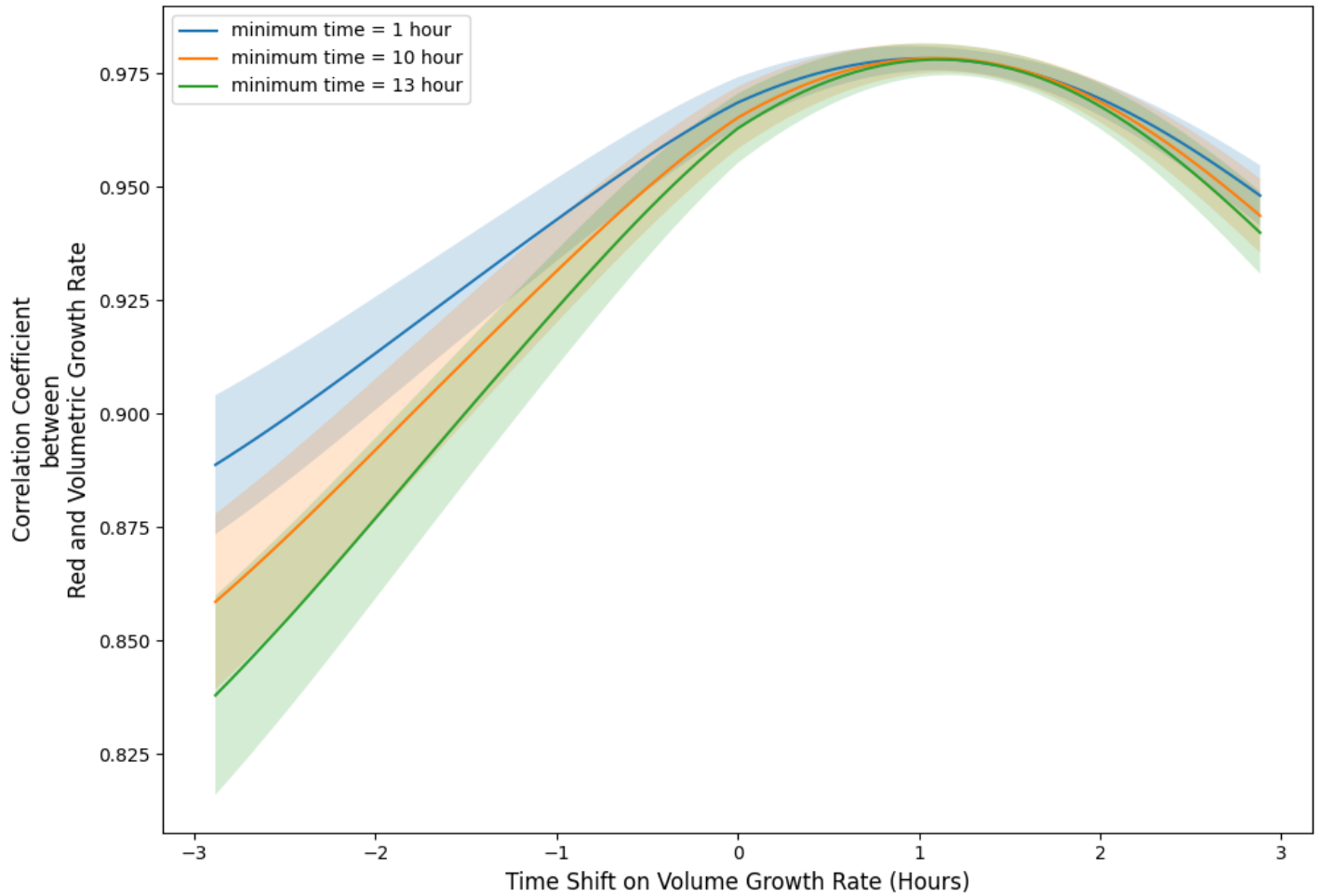
S15 Fig. Time Lag Analysis. Dynamics over all development for food intake rate and growth rate regressions were compared to determine the existing time lag between the two curves. The time shift was applied to the volume growth rate. A correlation coefficient was calculated for the new volume growth rate curve and the untouched red fluorescence regression curve for each bootstrap regression. The solid line corresponds to the mean of all the correlation coefficients over the bootstrapping iterations and the shaded regions correspond to the standard deviation. Due to the qualitatively different dynamics in L1, we calculated correlation for L1-L4 (blue), the second half of L1 -L4 (orange), and L2-L4 (green). All curves show that there is an overall time shift of +1 hour (meaning changes in volume growth rate precede changes in food intake rate), matching the L3-L4 curve in S14 Fig but still a <90% correlation with no time lag.

Response = Norm.Red

Terms	Df	Sum Sq	Mean Sq	F value	Pr(>F)	% Var Explained
hour	1	439.46	439.46	217762.01	0	54.34
replicate	6	165.82	27.64	13694.48	0	20.51
well	10	0.32	0.03	15.62	0	0.04
Residuals	100619	203.06	0	NA	NA	25.11

Response = Length

Terms	Df	Sum Sq	Mean Sq	F value	Pr(>F)	% Var Explained
hour	1	86190107879	86190107879	8223506	0	98.4
replicate	6	349438944	58239824	5557	0	0.4
well	10	834970	83497	8	0	0
Residuals	100619	1054582098	10481	NA	NA	1.2

Response = Width

Terms	Df	Sum Sq	Mean Sq	F value	Pr(>F)	% Var Explained
hour	1	209090438.47	209090438.47	6950760.3	0	97.99
replicate	6	1266985.87	211164.31	7019.7	0	0.59
well	10	1495.32	149.53	4.97	0	0
Residuals	100619	3026786.99	30.08	NA	NA	1.42

Response = Volume

Terms	Df	Sum Sq	Mean Sq	F value	Pr(>F)	% Var Explained
hour	1	6217124742191714688	6217124742191714688	843342	0	84.08
replicate	6	43356968850687072	7226161475114512	9802	0	5.86
well	10	152458715405862	15245871540586	21	0	0.02
Residuals	100619	74176459811167296	737201321929	NA	NA	10.03

961 **S1 Table. Results of analysis of variance models fit to COPAS BIOSORT data.** Analysis of variance tests
962 were used to quantify the amount of variance in our data contributed by the sampling technique. The sampling
963 technique involved unbiased sampling of animals from six replicate populations and subsequent distribution
964 into multiple wells of a microtiter plate for analysis. We quantified the amount of variance contributed by

965 replicate and well. We find that the variance explained by well is nearly negligible whereas replicate contributes
966 minor variance in some measurements. Given this information, we deem the generated summary statistics an
967 appropriate representation of the population.

Stage	ΔAIC			ΔBIC			Best model by AIC	Best model by BIC
	Linear	Exponential	Cubic	Linear	Exponential	Cubic		
L1_1	17	21	0	4	9	0	Cubic	Likely Cubic
L1_2	2	4	0	0	2	12	Can't distinguish	Can't distinguish
L2	142	43	0	128	28	0	Cubic	Cubic
L3	374	145	0	360	131	0	Cubic	Cubic
L4	4	44	0	0	40	10	Likely Cubic	Linear

968 **S2 Table. Model fit criteria used to assess candidate growth models.** To determine the level of support for
969 each model, the candidate model with the smallest raw AIC/BIC was identified and compared to other AIC/BIC
970 values. If the delta value was greater than 6, the model with the smallest AIC/BIC value was denoted as the
971 best model. If the delta value was less than 6 but greater than 2, the model with the smallest AIC/BIC value
972 was determined to likely be the best model. If the delta value was less than 2, we are unable to distinguish the
973 model of best fit.

Green Regions

Stage	Food Intake Dynamical Range (AFU)	Food to Growth Dynamical Range - Lower Estimate (AFU)	Food to Growth Dynamical Range - Higher Estimate (AFU)
L1 (1)	1	0	0
L1 (2)	1	2	2
L2	15	12	15
L3	29	21	27
L4	65	54	69

Red Regions

Stage	Food Intake Dynamical Range (AFU)	Food to Growth Dynamical Range - Lower Estimate (AFU)	Food to Growth Dynamical Range - Higher Estimate (AFU)
L1	--	--	--
L2	1	4	5
L3	6	3	4
L4	16	27	35

White Regions Preceding Molt

Stage	Food Intake Dynamical Range (AFU)	Food to Growth Dynamical Range - Lower Estimate (AFU)	Food to Growth Dynamical Range - Higher Estimate (AFU)
L1 -> L2	2	3	4
L2 -> L3	3	1	2
L3 -> L4	5	2	3
L4 -> Adult	5	2	3

Whole Larval Stage

Stage	Food Intake Dynamical Range (AFU)	Food to Growth Dynamical Range - Lower Estimate (AFU)	Food to Growth Dynamical Range - Higher Estimate (AFU)
L1	4	2	3
L2	19	12	15
L3	29	21	28
L4	70	52	67

974 **S3 Table.** Comparison of dynamical ranges between total food intake and food used for growth.

975 **S1 File. Incubator temperature data.** Temperature recordings of each position within the shaking incubator

976 used for the growth experiment. (CSV)

977 **S2 File. COPAS BIOSORT growth data.** Raw growth data collected from the COPAS BIOSORT and

978 processed using the *easysorter* R package to compile information from each well. (CSV)

979 **S3 File. Pruned COPAS BIOSORT growth data.** Processed data from the COPAS BIOSORT following

980 implementation of the *mclust* R package and removal of clusters containing non-animal objects. (CSV)

981 **S4 File. Image growth data.** Manual measurements of animal size acquired from images. (CSV)

982 **S5 File. Model derivations.**

1 Model Derivations

2 Bootstrapping Algorithm

3 To calculate a robust regression of the measured COPAS BIOSORT data we bootstrap the regression using

4 case-resampling (Davison and Hinkley 1997, pages 261-266). Each iteration of the algorithm (**Algorithm**

5 **S1**) involves resampling the data of interest with replacement and maintaining the size of the sample. At

6 each iteration the lokern regression is calculated for Red, Length, and Width data. Additionally any desired

7 function (for example, volume, pumping frequency times pharynx fraction, or derivatives) of these regressions

8 is calculated at each iteration. Regressions at each iteration are saved and the mean and variance of these

9 regressions at each regression time point are used to determine the statistics of the regression.

Algorithm S1 Regression Bootstrapping with Case Resampling

Ndata = # animals in sample;
iterations = # resamplings;

for $i = 0$ to iterations **do**
   Resample Ndata points with replacement. Collect Red, Length, Width data;

   Apply lokern regression to resampled Red, Length, Width;

   Calculate desired functions of Red, Length, Width regressions;

   Save Red, Length, Width, and combined regressions;
end for

Calculate Standard deviation at each regression time point of saved regressions;

---

10 Derivation of eating model

11 We begin by defining the instantaneous rate of food intake as a function of the flow rate of media through

12 the buccal cavity and the cross sectional area of the buccal cavity.

$$\frac{dV_{food}}{dt} = A_{buccal} \tag{S1}$$

13   We then make the assumption that the uptake of media fills the pharyngeal lumen we have

$$\frac{dV_{food}}{dt} = C\frac{dV_{lumen}}{dt} \tag{S2}$$

14   We average both sides of the equation under the assumption that the pumping period is significantly

15 shorter than the time scale of growth

$$\frac{1}{T}\int_0^T \frac{dV_{food}}{dt}dt = \frac{1}{T}\int_0^T CA_{buccal} \tag{S3}$$

16   The integral on the right hand side is the total food intake during a single pumping period.

$$\frac{1}{T}\int_0^T \frac{dV_{food}}{dt}dt = \frac{1}{T}\Delta V_{food} \tag{S4}$$

17   We then take into account that food is not transported to the gut in the same step as its uptake. Thus

18   the total food intake during a single pump can be calculated by the amount of food that fills the fully opened

19   pharyngeal lumen

$$\frac{1}{T}\int_0^T \frac{dV_{food}}{dt}dt = \frac{C}{T}V_{lumen:max} \tag{S5}$$

20   We then replace the average on the right hand side with the average food intake rate over the pumping

21   period. For simplicity and because we will deal entirely with the average food intake rate, we do not use a

22   different notation for this average rate.

$$\frac{dV_{food}}{dt} = \frac{C}{T}V_{lumen:max} = Cf(t)V_{lumen:max} \tag{S6}$$

Transformation of sorter measurements to volume units

24   To utilize sorter measurements and convert them to meaningful units we define a linear transformation from

25   the correlation plots (S1 Fig)

$$L = a_1 TOF + b_1 \tag{S7}$$

$$W = a_2 norm.EXT + b_2. \tag{S8}$$

26   Using Equations (S7) and (S8) we can approximate the volume of any object that passes through the

27   sorter by the expression

$$V = \frac{\pi}{4}(a_1 TOF + b_1)(a_2 norm.EXT + b_2)^2. \tag{S9}$$

Defecation analysis

We use the defecation results found in (Liu and Thomas 1994) to determine if red fluorescent measurements can be used as a proxy for food intake rate as opposed to the instantaneous food volume in the gut. Defecation in adults happens very regularly, with a period of $T_d = 45 \pm 3s$, with $h_d = 43 \pm 10\%$ of their intestinal volume being expelled each time. The volume expelled is well mixed. Defining V_f as the current amount of food in the nematode gut. We can use conservation of mass to state that the rate of change in the amount of food in the gut is equal to the rate of food intake through eating less the defecation rate and the rate at which food volume is metabolized into cell products:

$$\frac{dV_f}{dt} = \left.\frac{dV_f}{dt}\right|_{eating} - \left.\frac{dV_f}{dt}\right|_{defecating} - \left.\frac{dV_f}{dt}\right|_{metabolized} \tag{S10}$$

Using red fluorescence as a proxy for food intake we can ignore the metabolism term as the fluorescent beads are not metabolized.

$$\frac{dV_f}{dt} = \left.\frac{dV_f}{dt}\right|_{eating} - \left.\frac{dV_f}{dt}\right|_{defecating} \tag{S11}$$

Equation (S11) states that the rate of change of the volume of fluorescent beads in the gut is equal to the difference between the intake of red fluorescent beads minus the defecation rate of red fluorescent beads. Using the results of (Liu and Thomas 1994) for the second term, and defining $V_{f:max}$ as the volume of food in the gut just prior to defecation, h_d as the fraction of food expelled during a single defecation cycle, and T_d as the period of defecation. We average Equation (S11) over short time periods to remove the pumping and defecation period oscillations.

$$\frac{dV_{red:max}}{dt} = \left.\frac{dV_red}{dt}\right|_{eating} - \frac{V_{red:max}h_d}{T_d} \tag{S12}$$

On the left hand side, the instantaneous rate of the gut red fluorescence in Equation (S11) is replaced by the rate of change of the maximum or "full" gut fluorescence. The second term on the right hand side of Equation (S11) has been replaced by the average defecation rate over a cycle calculated by multiplying the full gut fluorescence by the fraction expelled and dividing by the defecation period. We solve Equation (S12) for the average eating rate.

$$\left.\frac{dV_{red}}{dt}\right|_{eating} = \frac{dV_{red:max}}{dt} + \frac{V_{red:max}h_d}{T_d} \tag{S13}$$

We take the local regression of the red fluorescence to determine $V_{red:max}(t)$. This value is plugged into

the second term on the right hand side of Equation (S13) and its derivative is used to approximate the first term on the right hand side of Equation (S13). We take the adult values of h_d and T_d (Liu and Thomas 1994) as a first approximation. Figure (S6) demonstrates a comparison of the red fluorescence and the red intake rate with defecation taken into account at the constant adult rates and quantities. We have scaled both the pink curve denoting red fluorescence and the blue curve denoting red intake rate by their maximum. This scaling allows us to see that the two curves are only a multiplicative factor apart up to error bars. This allows us to use the red measurement as a proxy for both red and food intake rates.

Food Allocation Breakdown Calculation

We calculate an example of resource allocation breakdown. We begin with the expression in Equation (8) of the main text relating food intake rate and animal growth rate and repeated here:

$$\frac{dV_{worm}}{dt} = \eta(t)\alpha(t)\frac{dV_{food}}{dt} \tag{S14}$$

Here $\eta(t)$ is metabolic efficiency and is characteristic of the nematodes and food source used. $\alpha(t)$ is the fraction of total ingested food allocated towards growth.

We make an additional assumption that food needed to maintain life is proportional to animal volume:

$$\frac{dV_{food:maint}}{dt} = \beta V_{worm}(t) \tag{S15}$$

Here we define $\frac{dV_{food:maint}}{dt}$ as the rate of food intake required to maintain life and β is the constant of proportionality that relates animal size to required maintenance food levels. We assume that β is a constant over developmental time and depends on the food source available.

From the analysis from the previous section we can use red fluorescence as a proxy for food intake rate such that

$$\frac{dV_{food}}{dt} \propto Red \tag{S16}$$

$$\frac{dV_{worm}}{dt} \propto \eta(t)\alpha(t)Red \tag{S17}$$

$$\eta(t)\alpha(t) \propto \left(\frac{dV_{worm}}{dt}\right)/Red \tag{S18}$$

The constant of proportionality in Equation (S18) is unknown due to the unknown relationship between food volume and red fluorescence. We make the assumption that metabolic efficiency is constant over time

70 and any variation in the value calculated by Equation (S18) is due to changes in $\alpha(t)$, the allocation of food

71 toward growth.

72   To calculate an estimate for the breakdown of food allocation, we assume a set of constants of propor-

73 tionality for Equations (S15) and (S18). We assume that at the time at which the $\eta(t)\alpha(t)$ curve is at its

74 maximum (hour 40), 10% of food resources are allocated towards maintenance, 70% (low growth estimate) or

75 90% (high growth estimate) are allocated towards growth, and the remainder is allocated to other metabolic

76 processes. The resulting scaling factors are applied over developmental time to calculate an estimated food

77 allocation breakdown and presented in Figure (8) of the main text.

Derivation of Stretcher Model

79 We model the cuticle as a thin walled pressure vessel made of orthotropic, linear materials to capture the

80 relationship between how much the cuticle stretches and the force applied to the cuticle. The relationship

81 between the amount of stretch and the amount of applied pressure is described by the matrix:

$$\begin{bmatrix} \varepsilon_L \\ \varepsilon_{Circ} \end{bmatrix} = \begin{bmatrix} \frac{1}{E_L} & \frac{-v_{cl}}{E_c} \\ \frac{-v_{lc}}{E_L} & \frac{1}{E_c} \end{bmatrix} \begin{bmatrix} \sigma_L \\ \sigma_{Circ} \end{bmatrix} \tag{S19}$$

82   Here E_L and E_C are the Young's modulus in the length and circumferential direction, and v_{cl} and v_{lc}

83 are the appropriate Poisson's ratios. These material properties can be measured experimentally. Normalized

84 stretch, ε, is defined as the change in size normalized by the initial size of a cuticle in length (L) and

85 circumference (Circ) (**Equations S20 - S21**) . Here σ is the normalized force applied along the length and

86 circumferential directions of the cuticle (**Equations S23 - S24**).

$$\varepsilon_L = \frac{\Delta L}{L_0} \tag{S20}$$

$$\varepsilon_{Circ} = \frac{\Delta Circ}{Circ_0} \tag{S21}$$

87   Here L_0 and $Circ_0$ are the length and circumference of the cuticle at the onset of stretch, or in other words

88 at the start of a larval stage. Experimentally we measure width, not circumference, but the circumference

89 of a circle is proportional to the width of the circle, so we can replace the circumference with the measured

90 width:

$$\frac{\Delta Circ}{Circ_0} = \frac{\pi \Delta W}{\pi W_0} = \frac{\Delta W}{W_0} \tag{S22}$$

By approximating *C. elegans* as cylindrical, and assuming the only force working on the cuticle is isotropic internal pressure, we can determine the normalized force in terms of pressure and geometric properties:

$$\sigma_L = \frac{r}{2t}\Delta p \tag{S23}$$

$$\sigma_{Circ} = \frac{r}{t}\Delta p \tag{S24}$$

Where r is the radius of the cylinder and t is the thickness of the cuticle. We can now rewrite Equation (S19) in terms of measurable quantities (length and width) by multiplying out the matrices making the appropriate substitutions.

$$\Delta L = \frac{L_0 r}{t}\left(\frac{1}{2E_L} - \frac{v_{cl}}{E_c}\right)\Delta p = a_L \Delta p \tag{S25}$$

$$\Delta W = \frac{W_0 r}{t}\left(\frac{1}{E_C} - \frac{v_{lc}}{E_L}\right)\Delta p = a_W \Delta p \tag{S26}$$

Here we compress the coefficients fixed by material and geometric properties into one constant

$$a_L = \frac{L_0 r}{t}\left(\frac{1}{2E_L} - \frac{v_{cl}}{E_c}\right) \tag{S27}$$

$$a_W = \frac{W_0 r}{t}\left(\frac{1}{E_c} - \frac{v_{lc}}{E_L}\right) \tag{S28}$$

Stretcher Slope Calculations

The Stretcher model predicts a constant ratio between stretch in width, ΔW, and stretch in length, ΔL. These measures of stretch are changes in the length and width measurements over some period of time. To see how the ratio of $\frac{\Delta W}{\Delta L}$ changes throughout a larval stage, we need to measure the stretch instantaneously. To do this we take advantage of the derivative approximation

$$\Delta W \approx \frac{dW}{dt}\Delta t \tag{S29}$$

$$\Delta L \approx \frac{dL}{dt}\Delta t \tag{S30}$$

Equations (S29, S30) are combined in the ratio found in Equation (3) to give:

$$\frac{\Delta W}{\Delta L} \approx \frac{W'(t)}{L'(t)} \tag{S31}$$

Here $W' = \frac{dW}{dt}$ and $L' = \frac{dL}{dt}$. We differentiate the time series from the local regressions of length and width data. The ratio of derivatives gives the instantaneous stretch ratio as it changes over time. Due to the numerical difficulty of calculating both derivatives and ratios with accuracy, we expect large error bars for this ratio. To estimate the size of error bars we apply a first order error propagation formula to Equation (S31).

$$\sigma^2_{Ratio} \approx \left|\frac{\partial Ratio}{\partial(W')}\right|^2 \sigma^2_{(W')} + \left|\frac{\partial Ratio}{\partial(L')}\right|^2 \sigma^2_{(L')} + 2\frac{\partial Ratio}{\partial(W')}\frac{\partial Ratio}{\partial(L')}\sigma_{(W')(L')} \tag{S32}$$

$$\sigma^2_{Ratio} \approx \left|\frac{1}{L'}\right|^2 \sigma^2_{(W')} + \left|\frac{-(W')^2}{(L')^3}\right|^2 \sigma^2_{(L')} - 2\frac{W'}{(L')^3}\sigma_{(W')(L')} \tag{S33}$$

The variance in Equation (S33) is calculated for each time point in the regressions of length and width. We resample the data for each larval stage 2,000 times with replacement (see Methods for larval stage determination). For each of these resampled sets of data, we numerically differentiate the length and width regression to determine an estimate of the length and width derivatives over time. At each time point the mean regression length and width derivatives are used in place of W' and L'. The covariance matrix for the length and width derivatives is calculated at each time point using the 2,000 resampled regressions in the bootstrap analysis and used as the variance terms in Equation (S33).